Multi-Variable Optimization of PEMFC Cathodes using an Agglomerate Model

M. Secanell [a], K. Karan [b], A. Suleman [a] and N.Djilali [a,*]

[a] *Institute for Integrated Energy Systems and Dept. Mechanical Engineering, University of Victoria, PO Box 3055 STN CSC, Victoria, BC, Canada, V8W 3P6*

[b] *Queen's-RMC Fuel Cell Research Centre and Dept. Chemical Engineering, Queen's University, Kingston, ON, Canada, K7L 3N6*

Abstract

A comprehensive numerical framework for cathode electrode design is presented and applied to predict the catalyst layer and the gas diffusion layer parameters that lead to an optimal electrode performance at different operating conditions. The design and optimization framework couples an agglomerate cathode catalyst layer model to a numerical gradient-based optimization algorithm. The set of optimal parameters is obtained by solving a multi-variable optimization problem. The parameters are the catalyst layer platinum loading, platinum to carbon ratio, amount of electrolyte in the agglomerate and the gas diffusion layer porosity. The results show that the optimal catalyst layer composition and gas diffusion layer porosity depend on operating conditions. At low current densities, performance is mainly improved by increasing platinum loading to values above $1mg/cm^2$, moderate values of electrolyte volume fraction, 0.5, and low porosity, 0.1. At higher current densities, performance is improved by reducing the platinum loading to values below $0.35mg/cm^2$ and increasing both electrolyte volume fraction, 0.55, and porosity 0.32. The underlying improvements due to the optimized compositions are analyzed in terms of the spatial distribution of the various overpotentials, and the effect of the agglomerate structure parameters (radius and electrolyte film) are investigated. The paper closes with a discussion of the optimized composition obtained in this study in the context of available experimental data. The analysis suggests that reducing the solid phase volume fraction inside the catalyst layer might lead to improved electrode performance.

Key words: fuel cell, catalyst layer, gas diffusion layer, platinum loading, sensitivity analysis, finite elements

* Corresponding author.
  Email addresses: `secanell@uvic.ca` (M. Secanell), `ndjilali@uvic.ca` (N.Djilali).

1 Introduction

Numerical modeling and optimization of catalyst layers remins one of the most challenging problems in polymer electrolyte membrane fuel cells (PEMFC's) because of the complex coupling of transport and reaction of chemical (hydrogen, oxygen, water) and charged species (electrons and ions) occurring in the complex composite porous structure. Due to the complexities of modeling such layers, several macroscopic catalyst layer models have emerged in the literature in the last decade with varying degrees of resolution and detailed representation or parameterization of the complex physico-electro-chemical processes [1–14]. These methods can be broadly classified in three categories: interface models, pseudo-homogeneous film models and agglomerate models [15].

Interface models which earlier models of complete fuel cells had to rely on due to computational costs [16,17] assume the catalyst layer to be infinitely thin and do not directly account for the layer composition and structure. The catalyst layer is regarded as an interface between the membrane and the gas diffusion layer and a single equation for the reaction kinetics is used to model the effect of the catalyst layer in the overall cell performance. This equation is introduced into the cell model as a boundary condition between the gas diffusion layer (GDL) and the membrane. Such models do not account for gradients in chemical species concentration and overpotential. This method has been used in most PEM fuel cell optimization studies to date [18–20], and as a result have not permitted optimization of the catalyst layer to be considered.

In pseudo-homogeneous film models, the catalyst layer is taken to be a porous structure consisting of a catalyst (usually platinum) supported on a solid conductive material (usually carbon) and an electrolyte (usually Nafion^{TM}). The reaction occurs on the surface of the catalytic particles supported on the solid conductive material, and therefore, ions, electrons and oxygen must transport through the catalyst layer to reach the reaction sites. In the cathode catalyst layer, electrons are transported through the solid conductive material, ions through the electrolyte, and oxygen through the void spaces. Two approaches are commonly used to represent oxygen transport. In the first, the void spaces are assumed to be flooded with water, and oxygen is assumed to transport in the dissolved state by diffusion [1–4]. In the second approach, oxygen is present in the gas phase within the pores of the wet-proofed catalyst layer, and transport is considered to take place by gas phase diffusion [5–9]. These two approaches result in drastically different resistance to oxygen transport. In the former case, oxygen is mostly consumed at the interface between the GDL and the catalyst layer; in the case of gas phase diffusion on the other hand, oxygen is distributed more homogeneously throughout the catalyst layer. Re-

gardless of the differences, both assumptions yield a model that takes into account some of the most important effects occurring at the catalyst layer as well as the composition of the catalyst layer by relating catalyst layer properties to the volume fraction of each material.

The agglomerate structure for catalyst layer models proposed some time ago by Ridge et al. [11], gained support with more recent microscopy observations [13,12] and several models have appeared using this structure [10–12,21]. Agglomerate models take the conductive carbon support and platinum particles to be grouped in small agglomerates bonded and surrounded by electrolyte, [10–12,21]. The agglomerates are assumed to be either cylindrical [11] or spheres of electrolyte -usually Nafion^{TM}- filled with carbon and platinum particles [13,12]. The reaction inside the agglomerate is then modeled as a reaction in a porous catalyst [22]. Oxygen is assumed to diffuse through the gas pores between agglomerates, dissolve into the electrolyte phase and finally diffuse through the electrolyte inside the agglomerate to the reaction site.

Several studies have shown that agglomerate models provide a better fit to experimental results [13,14], and a comprehensive comparative study of the three catalyst layer models was recently presented using three-dimensional numerical solutions [23]. This comparison highlighted the importance of a physically representative model for the catalyst layer, showing that, at low current densities, the thin film model results in different current density distributions compared to the pseudo-homogeneous and agglomerate models. Furthermore, only the agglomerate model was capable of predicting the performance drop at high currents due to mass transport limitations that is observed in an actual fuel cell. Based on these findings as well as the microscopy based evidence, the gradient-based optimization framework developed by the authors [24] and which was demonstrated using a pseudo-homogeneous model, has been improved by implementing an agglomerate model in order to achieve more realistic catalyst layer compositions.

Currently available manufacturing techniques only control the mass loading of each material used to create the catalyst layer ink [25]. The catalyst layer ink parameters however, are not used as input parameters to current agglomerate models and therefore, these models are not appropriate for optimization. In this paper, the agglomerate model described by Sun et al. [10] is modified in order to relate the catalyst layer ink composition to the catalyst layer properties. Next, this new model is implemented into the in-house finite element solver described in reference [24] to obtain numerical solutions, and the model sensitivity equations are derived with respect to all the design parameters. The model is then coupled to an optimization algorithm, and optimal catalyst layer compositions at several current densities are obtained. Finally, the results are analyzed and assessed in comparison to the optimal catalyst layer compositions obtained experimentally.

2   Mathematical model of the cathode electrode

In this section, a cross-the-channel two-dimensional mathematical model for a cathode electrode is described. The model is based on the following assumptions:

- The fuel cell is at steady state.
- It is at constant temperature and pressure.
- The gas diffusion layer is composed of void space and carbon fibers.
- The catalyst layer is formed by a mixture of carbon supported platinum, ionomer membrane electrolyte and void space.
- The electrochemical reaction occurs in the catalyst layer.
- The transport of reactants from the gas channels to the catalyst layer occurs only by diffusion of oxygen gas to the agglomerate surface and then by dissolution and diffusion through the ionomer to the reaction site.
- Oxygen gas transport in the GDL and the CL is modeled using Fick's first law instead of the Maxwell-Stefan equations to reduce the nonlinearity of the system of equations. Dilution effects are therefore not accounted for in the model, however, they are expected to be negligible since both oxygen and water are dilute species in nitrogen and their diffusion coefficients are similar.
- Water transport and its effect on membrane conductivity and potential for cathode flooding are not considered.

Using the assumptions above, the gas diffusion and catalyst layers are governed by the following set of equations [24]

$$
R(\mathbf{u}, \mathbf{p}) = \begin{cases} \nabla \cdot (c_{tot} D_{O_2}^{eff} \nabla x_{O_2}) - \frac{1}{4F} \nabla \cdot \mathbf{i} = 0 \\ \nabla \cdot (\sigma_m^{eff} \nabla \phi_m) - \nabla \cdot \mathbf{i} = 0 \\ \nabla \cdot (\sigma_S^{eff} \nabla \phi_S) + \nabla \cdot \mathbf{i} = 0 \end{cases} \tag{1}
$$

where R represents the residual, $\mathbf{u}$ the vector of unknowns which are the oxygen molar fraction x_{O_2}, the ionomer membrane electrical potential ϕ_m and the solid phase electrical potential ϕ_S. Finally, $\mathbf{p}$ represents the vector of design variables which will be discussed in section 3. These equations are solved for both the GDL and CL domains and, therefore, the system of equations fully couples these domains. Furthermore, the physical properties of the GDL and CL, oxygen diffusion coefficient, $D_{O_2}^{eff}$, proton conductivity, σ_m^{eff}, and electron conductivity, σ_S^{eff}, are related to the material composition. Similarly, the volumetric current density, $\nabla \cdot \mathbf{i}(x_{O_2}, \phi_m, \phi_S)$, is also dependent on the catalyst layer composition.

The volumetric current density is given by [10]

$$\nabla \cdot \mathbf{i} = 4F\frac{p_{tot}x_{O_2}}{H_{O_2,N}}\left(\frac{1}{E_rk_c(1-\epsilon_V^{cl})} + \frac{(r_{agg}+\delta_{agg})\delta_{agg}}{a_{agg}r_{agg}D_{O_2,N}}\right)^{-1} \quad (2)$$

where the different parameters are described in detail in section 2.5.

2.1 Conductivities in the gas diffusion layer and catalyst layer

The effective proton and electron conductivities, σ_m^{eff} and σ_S^{eff}, take different values in the GDL and catalyst layer. In the catalyst layer, σ_m^{eff} and σ_S^{eff} in (1), are obtained using Bruggeman relation to account for the porosity and tortuosity of the catalyst layer and are thus

$$\sigma_m^{eff-cl} = \sigma_m^{cl}(\epsilon_N^{cl})^{3/2} \quad (3)$$
$$\sigma_S^{eff-cl} = \sigma_S^{cl}(\epsilon_S^{cl})^{3/2} \quad (4)$$

In the gas diffusion layer, only solid phase and void space exist and therefore, the effective conductivities of protons and electrons are

$$\sigma_m^{eff-gdl} = \sigma_m^{gdl}(\epsilon_N^{gdl})^{3/2} \approx 0 \quad (5)$$
$$\sigma_S^{eff-gdl} = \sigma_S^{gdl}(\epsilon_S^{gdl})^{3/2} \quad (6)$$

It must be noted that in reality there is no proton conduction in the GDL. To avoid numerical difficulties in coupling fluxes at domain boundaries, the proton conduction equation is solved for both the GDL and the CL domains but protonic flux in the GDL is forced to be essentially zero by setting protonic conductivity to be nearly zero (ten orders of magnitude lower). In this paper, Bruggemann's equation is used to compute effective conductivities even though it was developed for granular media and the GDL is a media made of carbon fibers. Despite its shortcomings, Bruggemann's expression is widely used and there is not yet a universally accepted expression to estimate electron conductivity in the GDL as suggested in references [26,27].

2.2 Volume fraction of each phase in the catalyst layer

In order to compute the effective properties of the catalyst layer, the volume fraction of each material in the catalyst layer: solid, electrolyte and void space needs to be obtained. In the previous literature, either the effective properties were assumed directly or the volume fractions were given independently of the catalyst layer ink composition and effective parameters estimated using these

volume fractions, [7,10]. However, the catalyst layer ink composition dictates the amount of each one of these materials in the catalyst layer.

The solid phase volume fraction is given by the amounts of platinum and carbon in the catalyst layer. These values can be obtained from the platinum mass loading, m_{Pt} and the mass platinum to carbon ratio, $Pt|C$, that are used to make the catalyst layer ink. Both these values are known a priori and therefore, these should be used to compute the volume fraction in the solid phase. In our model, the solid phase volume fraction, ϵ_S^{cl}, is computed using [4]

$$\epsilon_S^{cl} = \left(\frac{1}{\rho_{Pt}} + \frac{1 - Pt|C}{Pt|C \rho_c} \right) \frac{m_{Pt}}{L} \tag{7}$$

where ρ_{Pt} and ρ_c are the platinum and carbon densities, $Pt|C$ is the platinum to carbon ratio, m_{Pt} is the platinum loading and L is the catalyst layer thickness. This last parameter is not known a priori but it can be controlled during the electrode preparation [28] or obtained a posteriori.

Assuming that the catalyst layer is made of spherical agglomerates and that the agglomerates are made only of ionomer and solid phase as shown in figures 1 and 2, then the total volume occupied by the solid phase in the catalyst layer can be related to the volume occupied by the agglomerates by

$$\epsilon_S^{cl} LH = \hat{n} \frac{4}{3} \pi r_{agg}^3 (1 - \epsilon_{agg}) \tag{8}$$

where L and H are the thickness and width of the catalyst layer, $\hat{n}$ is the number of agglomerates in the catalyst layer, r_{agg} is the radius of the agglomerate and ϵ_{agg} is the volume fraction of ionomer inside the agglomerate. Then, rearranging the expression above, the number of agglomerates per unit volume, n, can be expressed as

$$n = \frac{\hat{n}}{LH} = \frac{\epsilon_S^{cl}}{\frac{4}{3} \pi r_{agg}^3 (1 - \epsilon_{agg})} \tag{9}$$

In this equation, n represents the number of agglomerates per unit volume necessary to obtain the given volume fraction of solid phase. In this study, it is assumed that the agglomerates are made only of solid and electrolyte phases and have no void volume within an agglomerate. Further, it is assumed that the agglomerates are nearly spherical in shape but in fact they are not perfect rigid spheres. As a result, the agglomerates are assumed to conform within the specified catalyst volume in such a manner to generate the specified catalyst layer porosity, which exists as a result of inter-agglomerate void space only.

Once the number of spherical agglomerates is obtained, and assuming that all ionomer in the catalyst layer is present either in the bulk of the agglomerate
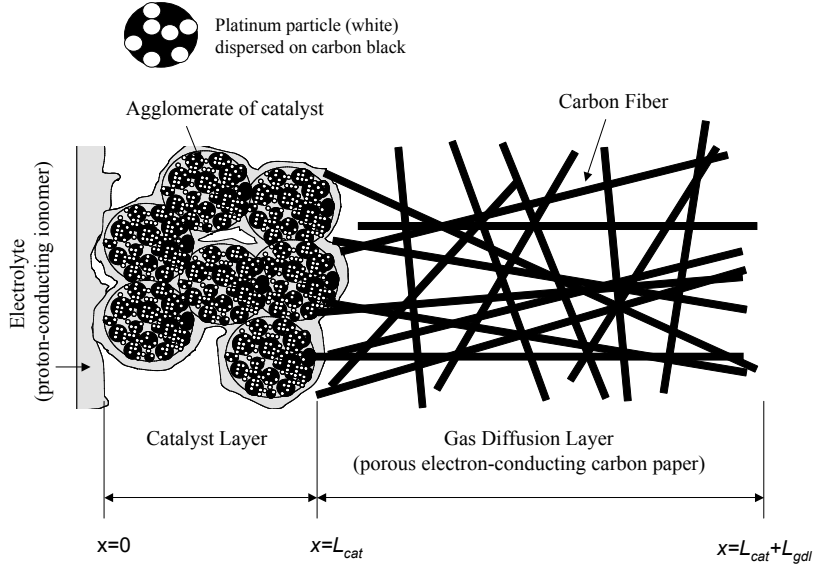
6

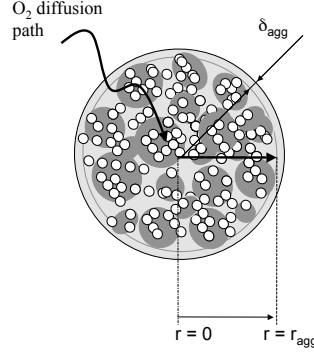Fig. 1. Catalyst layer and gas diffusion layer microstructure, [29]

Fig. 2. Agglomerate and thin film structure, [29]

or the thin film surrounding the agglomerate, as illustrated in figure 2, the electrolyte volume fraction in the catalyst layer can be obtained using geometrical arguments. The volume fraction of ionomer in the catalyst layer, ϵ_N^{cl}, is

$$\epsilon_N^{cl} = \frac{4}{3}\pi n [r_{agg}^3 \epsilon_{agg} + ((r_{agg} + \delta_{agg})^3 - r_{agg}^3)] \tag{10}$$

where δ_{agg} is the average thickness of the ionomer film surrounding the agglomerates. This expression is obtained by taking into account both the volume occupied by the electrolyte film and the volume of the agglomerate sphere occupied by the electrolyte.

7

Finally, once the volume fraction of solid phase and ionomer are obtained, the porosity of the catalyst layer is given by

$$\epsilon_V^{cl} = 1 - \epsilon_N^{cl} - \epsilon_S^{cl} \tag{11}$$

This equation gives the total porosity, i.e. the space that is occupied by neither the electrolyte nor the solid phase and that is represented in Figure 1 in white. This value should be interpreted as the volume fraction of the catalyst layer available for the formation of macro-pores for oxygen transport and not as the interstitial space between spheres.

This model differs from that of reference [10] in that the volume fractions in the catalyst layer are obtained as a function of the platinum loading m_{Pt}, the platinum to carbon weight ratio $Pt|C$, the thickness of the catalyst layer L, the radius of the agglomerate, r_{agg}, the volume fraction of ionomer, or electrolyte, inside the agglomerate, ϵ_{agg}, and finally, the ionomer thin film, δ_{agg}. In reference [10], the volume fraction and the other parameters are all given as an input paramete. Furthermore, the platinum to carbon ratio is not used even though it is typically an input variable when preparing the catalyst ink.

2.3   Oxygen transport to the surface of the agglomerate

The effective oxygen diffusion coefficient inside the catalyst layer in equation (1) is computed using the Bruggeman correction [4] to account for the effect of the porosity and conductive path tortuosity and is given by

$$D_{O_2}^{eff-gdl} = D_{O_2}(\epsilon_V^{gdl})^{3/2} \tag{12}$$
$$D_{O_2}^{eff-cl} = D_{O_2}(\epsilon_V^{cl})^{3/2} \tag{13}$$

where $D_{O_2}^{eff-gdl}$ and $D_{O_2}^{eff-cl}$ are the effective oxygen diffusion coefficients in the GDL and CL respectively.

Finally, in the GDL, ϵ_V^{gdl} represents the void space volume fraction. This value is related to the GDL solid phase by

$$\epsilon_V^{gdl} + \epsilon_S^{gdl} = 1 \tag{14}$$

In this paper, Bruggemann's equation is used to compute effective diffusivity even though it was developed for granular media and the GDL is a media made of carbon fibers. Currently, there is not yet a universally accepted expression to estimate the diffusivity in the GDL. Other suggested expressions can be found in references [26,27].

2.4 Oxygen dissolution and transport inside the agglomerate

Once the oxygen reaches the surface of the agglomerate, it dissolves into the electrolyte phase. To compute the concentration of oxygen in the electrolyte phase at the surface of the agglomerate, $c_{O_2,g|l}$, Henry's law is used

$$c_{O_2,g|l} = \frac{p_{O_2}}{H_{O_2,N}} \tag{15}$$

where $H_{O_2,N}$ is Henry's law constant and is $3.1664 \times 10^{10} \frac{Pa \cdot cm^3}{mol}$ in this article [10].

Next, once oxygen has dissolved into the electrolyte, it is transported by diffusion through the electrolyte film surrounding the agglomerate, Figure 2. The transport process is described by [10]

$$\hat{N}_{O_2} = D_{O_2,N}\frac{\partial c_{O_2}}{\partial r} = D_{O_2,N}\frac{r_{agg}}{r_{agg} + \delta_{agg}}\frac{c_{O_2,g|l} - c_{O_2,l|s}}{\delta_{agg}} \tag{16}$$

where $\hat{N}_{O_2}$ is the oxygen flux through the agglomerate boundary, $c_{O_2,l-s}$ is the concentration of dissolved oxygen at the agglomerate at the electrolyte solid interface and $D_{O_2,N}$ is the diffusion coefficient of oxygen in Nafion [10].

Finally, oxygen diffuses inside the agglomerate as it reacts. This transport process is given by

$$D^{eff}\frac{1}{r^2}\frac{\partial}{\partial r}\left(r^2\frac{\partial c_{O_2}}{\partial r}\right) = -c_{O_2}k_c \tag{17}$$

where k_c is the reaction rate computed using equation (23) and the diffusion coefficient inside the agglomerate, D^{eff}, is given by Bruggemann's relation

$$D^{eff} = D_{O_2,N}\epsilon_{agg}^{1.5} \tag{18}$$

Analytical integration of equation (17) yields an effectiveness factor, E_r, for the reaction inside the agglomerate such that the oxygen reaction in the catalyst layer can be written as [10]

$$R_{O_2} = (1 - \epsilon_V^{cat})E_r k_c c_{O_2,l|s} \tag{19}$$

where expressions for E_r and k_c are given in section 2.5.

Using this last equation, equations (15) and (16) and the mass balance of oxygen in the catalyst layer equations [10]

$$\nabla \cdot (c_{tot}D_{O_2}^{eff-cl}\nabla x_{O_2}) = a_{agg}\hat{N}_{O_2} \tag{20}$$

$$\nabla \cdot (c_{tot}D_{O_2}^{eff-cl}\nabla x_{O_2}) = R_{O_2} \tag{21}$$

the expression for the volumetric current density shown in section 2.5 is obtained. For a more detailed explanation, the reader is referred to reference [10].

2.5 Volumetric current density

The volumetric current density is [10]

$$\nabla \cdot \mathbf{i} = 4F\frac{p_{tot}x_{O_2}}{H_{O_2,N}}\left(\frac{1}{E_r k_c(1-\epsilon_V^{cl})} + \frac{(r_{agg}+\delta_{agg})\delta_{agg}}{a_{agg}r_{agg}D_{O_2,N}}\right)^{-1} \tag{22}$$

where

$$k_c = \frac{A_v i_0^{ref}}{4F(1-\epsilon_V^{cl})c_{O_2}^{ref}}\exp(-\frac{\alpha_c F}{RT}(\phi_s - \phi_m)) \tag{23}$$

where the term $1-\epsilon_V^{cat}$ is used to transform the active area in the catalyst layer, A_v to an active area inside the agglomerate and the effectiveness factor is given by

$$E_r = \frac{1}{\phi_L}\left(\frac{1}{\tanh(3\phi_L)} - \frac{1}{3\phi_L}\right) \tag{24}$$

and the Thiele's modulus for a spherical agglomerate is given by

$$\phi_L = \frac{r_{agg}}{3}\sqrt{\frac{k_c}{D^{eff}}} \tag{25}$$

where r_{agg} is the radius of the spherical agglomerate and D^{eff} is the effective oxygen diffusion coefficient inside the agglomerate. In case of a non-spherical agglomerate [22]

$$r_{agg} = 3\frac{V_{agg}}{S_{agg}} \tag{26}$$

where S_{agg} and V_{agg} are the external surface and volume of a single agglomerate respectively.

In these equations, there are several parameters that need to be obtained: $H_{O_2,N}$, a_{agg}, $D_{O_2,N}$, A_v, i_0^{ref}, $c_{O_2}^{ref}$ and D^{eff}. Parameters $H_{O_2,N}$, $D_{O_2,N}$, i_0^{ref} and $c_{O_2}^{ref}$ are input parameters to the model and are obtained from transport and electrochemical data. Parameters a_{agg}, A_v and D^{eff}, however, depend on the composition of the catalyst layer.

The parameter a_{agg} is defined as the ratio between the effective surface area usable to dissolve oxygen into the agglomerate and the catalyst layer volume. This value can be related to the catalyst layer structure by

$$a_{agg} = n4\pi(r_{agg}+\delta_{agg})^2\epsilon_V^{cl} \tag{27}$$

10

where n is the number of agglomerates per unit volume, the term $4\pi(r_{agg} + \delta_{agg})^2$ is the surface of a single agglomerate and finally, ϵ_V^{cl} is the catalyst layer porosity. The catalyst layer porosity is used to compute the effective surface area available for gas dissolution into the ionomer. That is, only the fraction of the surface of the agglomerate in contact with the gas pore is able to dissolve oxygen. Thus, since the pores exists only as inter-agglomerate volume increasing the porosity also results in an increase in exposed surface of the agglomerate. This can be visualized as an increase in the volume of the white space in Figure 1. In the extreme case of zero porosity, the catalyst layer would only contain cubical agglomerates packed together. Since there would be no space for the pores to connect to the surface, the oxygen dissolution into the agglomerates would be zero in this case. Similarly, if the porosity were close to unity, the agglomerates would be almost completely separated from each other by gas pores and only connected by small strings of electrolyte. In this case all the surface area of the agglomerate would be available for oxygen dissolution.

The parameter A_v represents the total catalytic area available for the oxygen reduction reaction per unit volume of catalyst layer. This value is related to the platinum loading, to the platinum particle size and to the platinum to carbon ratio. To account for the dependance of this value to platinum loading we write

$$A_v = A_0 \frac{m_{Pt}}{L} \tag{28}$$

where A_0 is the total catalyst surface area per unit mass of the catalyst particle. This value depends on the size of the platinum particles and on the platinum content of the catalytic particles in the catalyst layer. In this study, a least squares fit to the empirical data provided by Marr et al. [3] for different platinum supported catalysts is used to estimate this value

$$A_0 = 2.2779 \times 10^6 (Pt|C)^3 - 1.5857 \times 10^6 (Pt|C)^2$$
$$- 2.0153 \times 10^6 Pt|C + 1.5950 \times 10^6 \tag{29}$$

Note that as the platinum to carbon ratio increases the size of the platinum particles increases. Several factors including Pt precipitation/crystallization kinetics and Pt particle agglomeration are responsible for this phenomenon.

2.6   Boundary conditions

The PEM fuel cell electrode is sandwiched between the membrane and the bipolar plates. For this reason, and taking into account symmetry, the geometric domain of the model takes into account a computational domain that is half under the gas channel and half under the current collector as shown in Figure 3. From the figure, it is possible to distinguish four different boundary conditions:
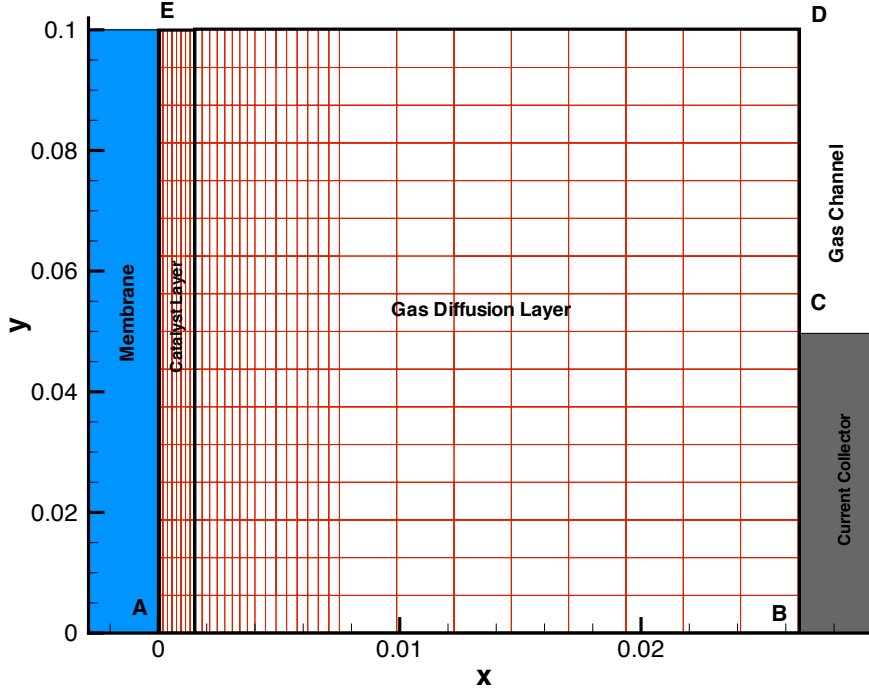
Fig. 3. Computational domain used to solve the equations of the cathode electrode model

- membrane at $(x, y) = \{x = 0, \forall y\}$,
- symmetric boundaries at $(x, y) = \{\forall x, y = 0 \text{ and } 0.1 cm\}$,
- current collector at $(x, y) = \{x = L + L^{gdl}, y = [0, 0.05]\}$, and
- gas channel at $(x, y) = \{x = L + L^{gdl}, y = [0.05, 0.1]\}$.

The boundary conditions at the membrane/electrode interface are

$$\mathbf{n} \cdot \nabla x_{O_2} = 0 \tag{30}$$
$$\mathbf{n} \cdot \nabla \phi_S = 0 \tag{31}$$
$$\phi_m = \phi_0 = dV \tag{32}$$

where $\mathbf{n}$ is the normal to the domain surface in contact with the membrane and ϕ_0 is the applied voltage to the electrode.

The boundary conditions at the symmetric faces are

$$\mathbf{n} \cdot \nabla x_{O_2} = 0 \tag{33}$$
$$\mathbf{n} \cdot \nabla \phi_S = 0 \tag{34}$$
$$\mathbf{n} \cdot \nabla \phi_m = 0 \tag{35}$$

The boundary conditions at the rib or current collector/electrode interface reflect the fact that the cathode is taken as the reference potential and are

$$\mathbf{n} \cdot \nabla x_{O_2} = 0 \tag{36}$$
$$\phi_S = 0 \tag{37}$$
$$\mathbf{n} \cdot \nabla \phi_m = 0 \tag{38}$$

Finally, the boundary conditions at the gas channel/electrode interface are

$$x_{O_2} = x_{O_2}^0 \tag{39}$$
$$\mathbf{n} \cdot \nabla \phi_S = 0 \tag{40}$$
$$\mathbf{n} \cdot \nabla \phi_m = 0 \tag{41}$$

where it is assumed that the concentration on the pores of the GDL is the same as the concentration of the mixture in the gas channel.

3   The Optimization Problem and Sensitivity Analysis

Fuel cell performance is commonly described in terms of its polarization behavior, i.e. voltage versus current density. Therefore, if the goal is to optimize fuel cell performance at a given operating point, i.e. at a fixed cell voltage, it is necessary to find the optimal catalyst layer and GDL compositions that produce the maximum current density. In the model described above, the catalyst layer composition is described by five parameters: the platinum loading, m_{Pt}, the mass percentage of platinum catalyst on the support carbon black, $Pt|C$, the agglomerate radius, r_{agg}, the agglomerate thin film thickness, δ_{agg} and the electrolyte volume fraction inside the agglomerate, ϵ_{agg}. Three of these parameters are used as design variables since it is assumed that they can be controlled. The platinum loading and the platinum to carbon ratio can be controlled by controlling the amount of catalyst in the ink and by selecting the appropriate catalytic particles. Manufacturers usually provide customers with a selection of catalytic particles with different platinum to carbon ratios [3]. The ionomer film and the amount of ionomer inside the agglomerate provide the total amount of electrolyte in the catalyst layer. However, it is difficult to discern how much of the electrolyte will become part of the agglomerate and how much it will be used to create an electrolyte film. A study performed by Lee et al. [30] suggests that the thickness of the electrolyte film surrounding the agglomerate increases rapidly when the electrolyte content in the catalyst layer increases from zero to 10%wt. and then remains almost constant. Following Lee et al., in this work it is assumed that the electrolyte film surrounding the catalyst layer is constant and equal to $80nm$. This film value

Table 1
Initial upper and lower bounds for the design parameters used to optimize the catalyst layer

Design variable	Upper bound	Lower bound
$m_{Pt}, [mg/cm^2]$	1.25	0.01
$\epsilon_{agg}, [-]$	0.9	0.1
$Pt|C, [-]$	1.0	0.1
$\epsilon_V^{gdl}, [-]$	0.9	0.1

should be adjusted depending on the method of preparation of the catalyst layer. Finally, the radius of the agglomerate is also considered constant, even though, Song et al. [31] suggest that this value can also be controlled by using different manufacturing processes and ink preparations. The effect of the agglomerate radius and the thickness of the film surrounding the agglomerate on the optimum catalyst layer design will be studied in detail in section 4.5.

3.1 The optimization problem

The optimization problem is formulated as

$$\text{maximize } i(\phi_0 = dV) \tag{42a}$$
$$\text{w.r.t. } m_{Pt}, \epsilon_{agg}, Pt|C, \epsilon_V^{gdl} \tag{42b}$$
$$\text{subject to: } 0 < \epsilon_V^{cl} < 1 \tag{42c}$$
$$0 < \epsilon_S^{cl} < 1 \tag{42d}$$
$$0 < \epsilon_N^{cl} < 1 \tag{42e}$$

The constraints guarantee that the volume fraction of each one of the three phases on the catalyst layer is not negative or larger than one. Bounds are also set on each one of the design variables. The design variable bounds are shown in Table 1. The most important bound is the upper bound for the platinum loading, which is constrained by cost. In this case, this value is set to $1.25 mg/cm^2$ which is almost twice that of currently used platinum loadings [25]. Note that if this upper value is increased, this might change the optimal solution. In fact, our simulations showed a second optimal solution for high platinum loadings and high ratios of platinum to carbon, i.e. 0.9. This second optimum is disregarded because it requires excessive amounts of platinum and it is not discussed here. Future work will aim to solve a multi-obejctive optimization problem that will simultaneously minimize platinum loading and maximize performance.

In the optimization problem above, the objective function is given by the fuel cell current density at a given electrode voltage. Current density is obtained during postprocessing. The current density per unit area of a fuel cell can be obtained by integrating the volumetric current density over the volume of the CL,

$$f(\mathbf{u}, \mathbf{p}) = i(x_{O_2}, \phi_S, \phi_m; m_{Pt}, \epsilon_{agg}, Pt|C, \epsilon_V^{gdd}) = \frac{1}{H} \int_0^H \int_0^L \boldsymbol{\nabla} \cdot \mathbf{i} \, dx dy \quad (43)$$

where $\boldsymbol{\nabla} \cdot \mathbf{i}$ is given in equation (2), H is the height of the domain and L is the width of the domain, i.e. the thickness of the CL. Furthermore, the constraint equations in the optimization problem in (42) are directly given by the analysis model. Hence, no extra computations are required to determine the constraints.

The analytic sensitivities of the objective function f, with respect to any of the design variables p_i, can be obtained using functional analysis as

$$\frac{df(\mathbf{u}, \mathbf{p})}{dp_i} = \frac{\partial f(\mathbf{u}, \mathbf{p})}{\partial u_j} \frac{\partial u_j}{\partial p_i} + \frac{\partial f(\mathbf{u}, \mathbf{p})}{\partial p_i}$$
$$= \frac{1}{H} \int_0^H \int_0^L \left(\frac{\partial(\boldsymbol{\nabla} \cdot \mathbf{i})}{\partial u_j} \frac{\partial u_j}{\partial p_i} + \frac{\partial(\boldsymbol{\nabla} \cdot \mathbf{i})}{\partial p_i} \right) dx dy \quad (44)$$

where $\mathbf{u}$ is the vector of unknowns solved for by the analysis program, $\mathbf{p}$ is the vector of design parameters, $i = 1, \ldots, 4$, $j = 1, \ldots, 3$, $\frac{\partial(\boldsymbol{\nabla} \cdot \mathbf{i})}{\partial u_j}$ and $\frac{\partial(\boldsymbol{\nabla} \cdot \mathbf{i})}{\partial p_i}$ are obtained by analytical differentiation of equation (2) with respect to the solution vector and the design variables respectively and, finally, the term $\frac{\partial u_j}{\partial p_i}$ is unknown and represents the change of the solution vector with respect to the design variables. This vector can be obtained by noticing that the residual of the governing equations has to be zero at the solution and that any perturbation in the parameters of the system should result in no variation of the residual if the governing equation is to be satisfied. Therefore, the total derivative of the residual has to be zero. Then, $\frac{\partial u_j}{\partial p_i}$ is computed by solving the system of partial differential equations given by

$$\frac{\partial R(\mathbf{u}, \mathbf{p})}{\partial u_j} \frac{\partial u_j}{\partial p_i} = -\frac{\partial R(\mathbf{u}, \mathbf{p})}{\partial p_i} \quad (45)$$

where $\frac{\partial R(\mathbf{u},\mathbf{p})}{\partial u_j} \frac{\partial u_j}{\partial p_i}$ and $\frac{\partial R(\mathbf{u},\mathbf{p})}{\partial p_i}$ represent the derivatives of the governing equations in (1) with respect to the solution vector and the design variables respectively. These are obtained using functional analysis. Note that $\frac{\partial R(\mathbf{u},\mathbf{p})}{\partial u_j} \frac{\partial u_j}{\partial p_i}$ is a directional derivative and therefore results in a differential equation with the vector $\frac{\partial u_j}{\partial p_i}$ as the unknown [32,33]. For example, for design variable p_i, from

the first term of equation (1),

$$\frac{\partial R_1(\mathbf{u}, \mathbf{p})}{\partial u_j} \frac{\partial u_j}{\partial p_i} = \nabla \cdot \left(c_{tot} D_{O_2}^{eff} \nabla \left(\frac{\partial x_{O_2}}{\partial p_i} \right) \right) - \frac{1}{4F} \frac{\partial (\nabla \cdot \mathbf{i})}{\partial u_j} \Bigg|_{u=u^n} \frac{\partial u_j}{\partial p_i} \qquad (46)$$

Once an analytic expression for these terms is obtained, the system of PDEs is discretized using the finite element method and the *deal.ii* finite element libraries [34] with appropriate boundary conditions. In this case, the boundary conditions for the unknown vector $\frac{\partial u_j}{\partial p_i}$ are Newmann boundary conditions with value set to zero. After discretization and application of the boundary condition, the resulting linear system is solved using UMFPACK [35,36], an efficient direct solver for nonsymmetric linear systems. The terms $\frac{\partial R(\mathbf{u}, \mathbf{p})}{\partial u_j}$ and $\frac{\partial R(\mathbf{u}, \mathbf{p})}{\partial p_i}$ depend on the solution of the governing equations and therefore this system of equations can only be solved after solving the governing equations as shown in figure 4. Finally, note that this system has the same size as the original linearized system of governing equations and that it needs to be solved for each design variable p_i. This method of obtaining the analytic sensitivities is the so-called direct formulation chosen here instead of the adjoint formulation because of its ease of implementation. A similar approach to compute sensitivities was also used in reference [37] to solve a least squares problem to estimate fuel cell model parameters from experimental data. As the number of design variables increases the adjoint formulation is proven to become more efficient [38].

Once the analytic sensitivities were implemented in the code, they were validated by comparing them to the numerical sensitivities computed using forward differences. Table 2 shows the results from the validations, performed using the data from Table 3 and with $dV = 0.5V$. Table 2 shows good agreement between analytic and numeric sensitivities.

Table 2
Analytic vs numeric sensitivities of the current density w.r.t. the different design variables

Design variable	Analytic	Numeric $(\delta h = 10^{-3})$	Numeric $(\delta h = 10^{-5})$	Numeric $(\delta h = 10^{-7})$
m_{Pt}	5.09198	5.19913	5.09303	5.09199
ϵ_{agg}	3.88996	3.97101	3.89075	3.88996
$Pt|C$	-10.0333	-9.62504	-10.0291	-10.0332
ϵ_V^{gdl}	-0.427460	-0.426597	-0.427452	-0.427458

3.3 Implementation of the optimization program

The electrode finite element model together with the analytic sensitivities of the objective function and constraints are coupled to the optimization package DAKOTA [39], as shown in Figure 4. In this figure, the three main iterative loops can be identified. The inner or analysis loop, is used to solve the nonlinear governing equations. The middle or adaptive refinement loop, is used to check the accuracy of the solution and adapt the computational mesh as necessary using an *a posteriori* error estimator. The outer or optimization loop, is used to change the design parameters in order to obtain an improved design. The stopping criteria for the nonlinear, adaptive and optimization loops is as follows: a residual smaller than 10^{-10}, an adaptive grid with more than 6,000DOF and a relative change in the objective function of less than 10^{-4}. An adapted grid with approximately 6,000 DOF yields a grid independent solution that can only be achieved by using a globally refined grid with approximately 20,000 DOF therefore resulting in large computational savings as can be seen in Figure 5.

The structure of the framework is similar to that reported in [24] and the reader is referred to the article for more details. However, several improvements have been included in this study. The linear solver has been update to UMFPACK [35,36,34], a direct solver for nonsymmetric linear systems. The Newton loop has been improved by including a step size test and the convergence criteria is now based on the norm of the residual instead of the relative change on the solution update. This make the code more accurate, robust and reliable. The sensitivity analysis calculations are removed from the adaptive refinement loop and are only performed at the last grid level. This improves the efficiency of the code by removing additional sensitivity computations that were unnecessary. Also, the *a posteriori* error estimator has been modified since the last publication. Finally, a new optimization package has been added to the framework, namely DAKOTA, [39]. This is because DAKOTA provides modern, accurate and reliable solvers as well as solvers for non-gradient based optimization and reliability based optimization. Furthermore, DAKOTA is OpenSouce software, therefore, allowing the authors the ability to modify any part of the design framework.

4 Optimization Results

The optimization problem outlined in equation (42) is solved in this section for three different voltages across the cathode: a low (0.3V), medium (0.5V) and high (0.7V) voltage which corresponds to a low, medium and high cell current density. For each one of these cases, the data in Table 3 is used as the
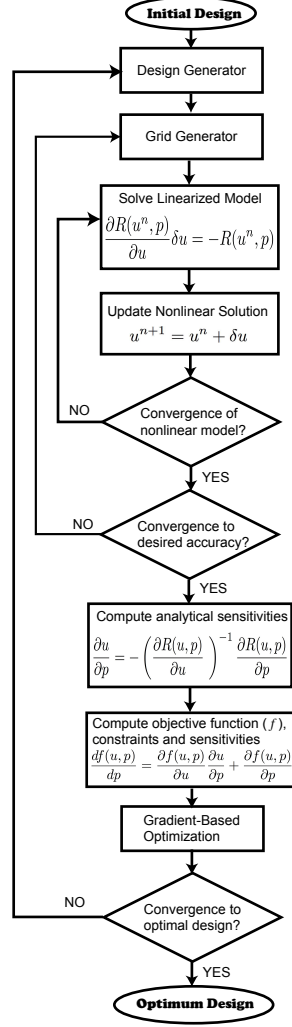
Fig. 4. Implementation of the multivariable optimization framework with adaptive refinement and analytic sensitivities.

initial design to begin the numerical optimization process. Then, the effect of the agglomerate structural parameters, i.e. radius of the agglomerate and thickness of electrolyte film surrounding agglomerate, on the performance and optimal electrode compositions are studied. Finally, the optimization results obtained from the agglomerate model are compared to previously published experimental data [40,41,30,42,43,28,44].

4.1 Base design

In this section, results are presented showing the performance of the base design which is presented in Table 3. For this initial design the CL solid, electrolyte and void phase volume fractions are 0.3552, 0.5398 and 0.1049,

18
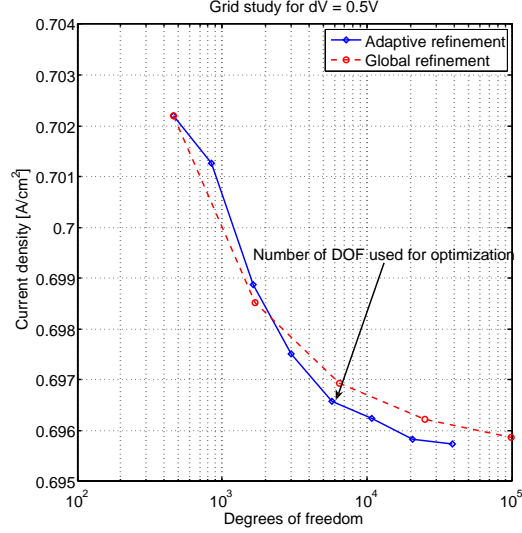
Fig. 5. Grid study at a voltage across the electrode of 0.5V using adaptive grid refinement (solid line) and global refinement (dashed line)

respectively. This data is based on the data given by references [10] and [24]. The polarization curve for this model is shown in Figure 6. In this figure, the cathode potential is plotted with respect to the cell current density. The cathode potential is defined as

$$V = E_{th} - dV \tag{47}$$

where dV is the voltage across the electrode, i.e. the overpotential, and E_{th} is the theoretical cathode voltage or potential in Volts and is given by [10]

$$E_{th} = 1.229 - 8.456 \times 10^{-4}(T - 298.15)$$
$$+ 4.31 \times 10^{-5}T(ln(p_{H_2}) + \frac{1}{2}ln(p_{O_2})) \tag{48}$$

In this case, assuming a pressure and relative humidity at both anode and cathode of 1.5atm and 50%, the partial pressures for hydrogen and oxygen are $p_{H_2} = 1.226atm$ and $p_{O_2} = 0.266atm$. Therefore, E_{th} is 1.1760V.

Figures 7, 8 and 9 show the oxygen molar fraction, solid and electrolyte phase potentials, the volumetric current density, $\nabla \cdot \mathbf{i}$ and the final adaptive grid at the catalyst layer for the base design. For these three cases, the current density is 0.1556, 0.6966 and 0.9312 A/cm^2 respectively. By comparison, the shape of

19

Table 3
Base case to perform catalyst layer optimization

Geometry			
thickness GDL, [cm]	2.5×10^{-2}, [10]	thickness cat, [cm]	1.5×10^{-3}, [10]
thickness channel, [cm]	0.1, [10]	thickness rib, [cm]	0.1, [10]
Operating conditions			
p, [atm]	1.5, [10]	T [K]	353, [10]
x_{O_2}	0.177310	x_{N_2}	0.66704
x_w	0.15565		
Physical properties			
D_{O_2}, $[cm^2 \cdot s^{-1}]$	0.1827, [45]	$H_{O_2,N}$, $[\frac{Pa \cdot cm^3}{mol}]$	3.1664×10^{10}, [10]
$D_{O_2,N}$, $[cm^2 \cdot s^{-1}]$	8.45×10^{-6}, [10]		
σ_S^{gdl}, $[S \cdot cm^{-1}]$	100	ϵ_V^{gdl}	0.5
σ_S^{cl}, $[S \cdot cm^{-1}]$	32.64, [24]	σ_m, $[S \cdot cm^{-1}]$	0.0263, [10]
α	0.61, [10]		
n	4, [10]	γ	1.0, [10]
i_0^{ref}, $[A \cdot cm^{-2}]$	1.5×10^6, [10]	$c_{O_2}^{ref}$, $[mol \cdot cm^{-3}]$	0.85×10^{-6}, [10]
ρ_{Pt}, $[g \cdot cm^{-3}]$	21.5, [4]	ρ_c, $[g \cdot cm^{-3}]$	2.0, [4]
ρ_N, $[g \cdot cm^{-3}]$	2.0, [4]	δ_{agg}, [nm]	80, [10]
m_{Pt}, $[mg/cm^2]$	0.4, [4]	$Pt|C$, [-]	0.28
r_{agg}, $[\mu m]$	1, [10]	ϵ_{agg}, [-]	0.5, [10]

the contour lines for the oxygen molar fraction and the solid phase potential remain almost unchanged for all three cases even though their gradients become larger as the voltage across the electrode is increased. On the other hand, large differences can be observed in the shape of the contour lines as well as in the gradient of the contour lines for the electrolyte phase potential and the volumetric current density. The electrolyte phase potential changes from having a distribution that was uniform in the y direction, to a more non-uniform distribution that changes on both coordinate directions and with smaller potentials under the channel. On the other hand, the volumetric current density follows a pattern similar to the one reported by Sun et al. [10]. At low currents, the current density is uniformly distributed throughout the catalyst layer, but as the current increases, the volumetric current density becomes less uniform and for a voltage across the electrode of 0.7V, the volumetric current density under the channel is substantially higher that under the land area. Finally, the three figures show the final adaptive grid. The figures illustrate the ad-
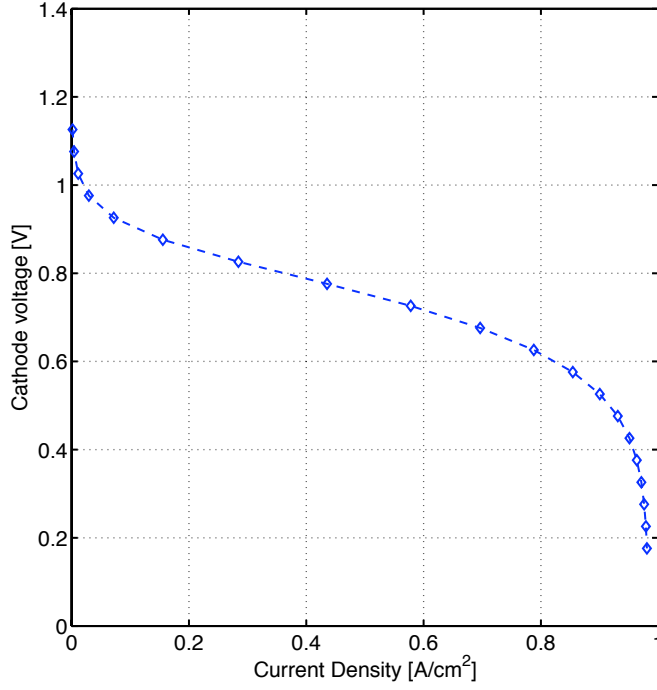
Fig. 6. Polarization curve for the current model

vantage of using adaptive grid refinement. The adaptive algorithm refines the computational mesh to resolve more accurately the areas with higher current densities.

In this article, optimum catalyst layer and GDL compositions are obtained using the agglomerate model in contrast to the author's previous work and the work of other research groups [24,4]. To be able to show the advantage of using the agglomerate model instead of the pseudo-homogeneous model, a polarization curve for the base design is created using the latter model and compared to the agglomerate model in Figure 10. To create the polarization curve for the pseudo-homogeneous case, the data in Table 3 is used as the input parameters. In the pseudo-homogeneous case, however, all the agglomerate parameters such as thickness of the electrolyte film surrounding the agglomerate are not used. Furthermore, for the pseudo-homogeneous model, the total volume fraction of electrolyte in the catalyst layer is used as a design parameter, instead of the amount of electrolyte inside the agglomerate. Using the agglomerate model, the total volume fraction of electrolyte in the catalyst layer is obtained using equation (10) and its value for the base design is 0.5398.

Comparing the polarization curves in Figure 10, it is easy to observe the large differences at high currents. While the agglomerate model results in moderate current densities at low voltages, the pseudo-homogeneous model
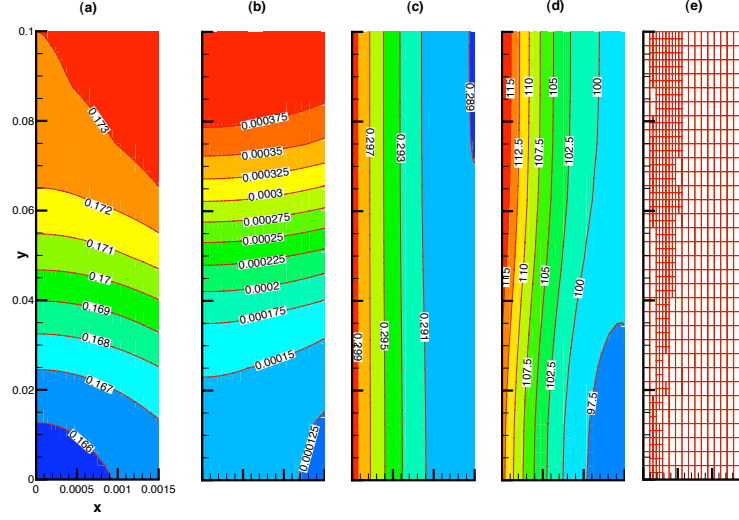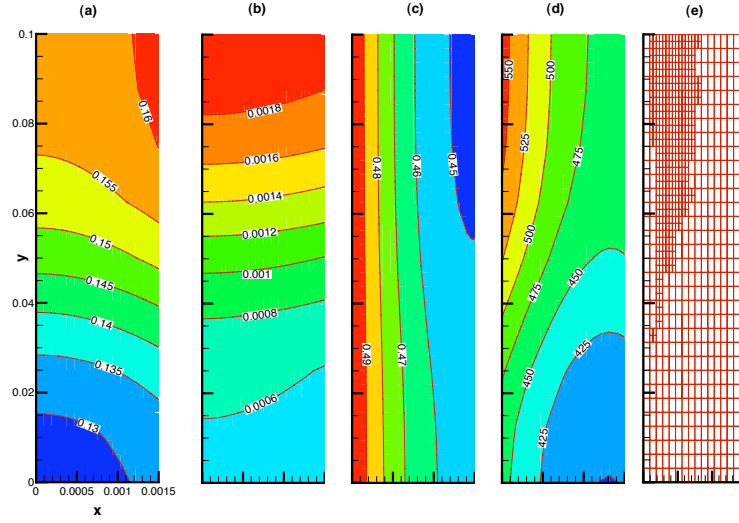
21

Fig. 7. Contour lines at the catalyst layer for the base electrode design at $dV = 0.3V$ for (a) oxygen molar fraction [-], (b) potential in the solid phase [V], (c) potential in the electrolyte [V], (d) volumetric current density [A/cm^3] and (e) final adaptive grid in the catalyst layer.

Fig. 8. Contour lines at the catalyst layer for the base electrode design at $dV = 0.5V$ for (a) oxygen molar fraction [-], (b) potential in the solid phase [V], (c) potential in the electrolyte [V], (d) volumetric current density [A/cm^3] and (e) final adaptive grid in the catalyst layer.

results in unrealistically high current denities. This difference is a result of the ability of the agglomerate model to predict the mass transport limitations due to the dissolution of oxygen into the agglomerate and the diffusion of oxygen inside the agglomerate which the pseudo-homogeneous model does
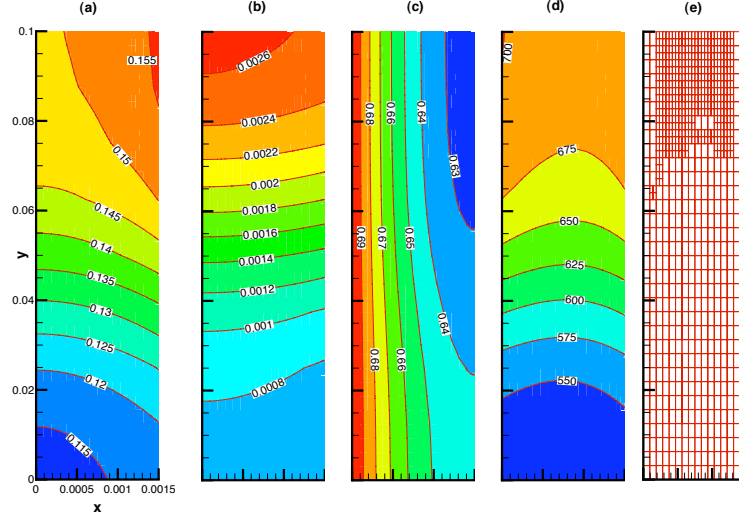
22

Fig. 9. Contour lines at the catalyst layer for the base electrode design at $dV = 0.7V$ for (a) oxygen molar fraction [-], (b) potential in the solid phase [V], (c) potential in the electrolyte [V], (d) volumetric current density $[A/cm^3]$ and (e) final adaptive grid in the catalyst layer.

not account for. This results are also in accordance with the results shown in reference [23]. The unrealistic current densities at low voltages make the pseudo-homogeneous model only applicable at low current densities and it is only in this range that optimization of the catalyst layer can be performed using the authors' previous model [24]. The agglomerate model on the other hand, allows for the optimization of the catalyst layer in the complete range of operating conditions.

4.2 Optimization at low current densities

The initial design provides a current density of $0.1556A/cm^2$ at an electrode voltage of 0.3V. Starting with this electrode design, the optimization problem outlined in equation (42) is solved using the quasi-Newton interior-point method in DAKOTA [39]. After 10 iterations and approximately 1 minute on a 2 GHz Power Mac G5, the optimization algorithm converged to a new design that provides a current density of $0.1936A/cm^2$. The design variables at this new design are $\{m_{Pt}, \epsilon_{agg}, Pt|C, \epsilon_V^{gdl}\} = \{1.1321, 0.3406, 0.4670, 0.7257\}$. For these values, the volume fractions of solid, electrolyte and void phase are 0.4658, 0.4240 and 0.1109 respectively. Finally, the gradient of the objective function is $\nabla_\lambda \cdot \mathbf{i} = \{-1.59e - 5, -4.03e - 5, 6.85e - 5, -4.55e - 6\}$ which results in a L_2 norm of 8.111e-5, i.e. almost zero. A zero gradient provides the mathematical proof that the solution is indeed a local optimum. A mathematical proof of a global optimum is not available, however, parametric studies
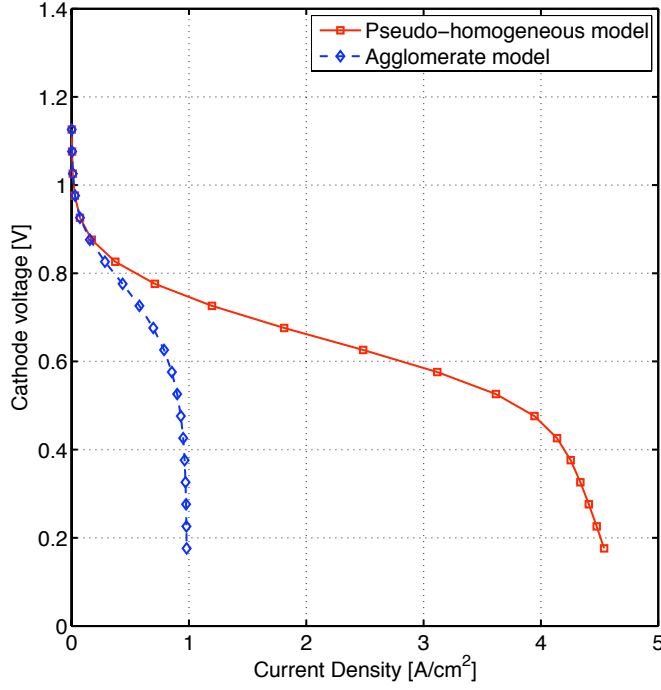
Fig. 10. Polarization curve for the base design analyzed using the agglomerate model and the pseudo-homogeneous model.

and optimization starting from other initial points show that this solution is most likely a global solution. Another optimum design is also observed outside the design space for $Pt|C$ of 90% and a platinum loading larger than the maximum bound.

Comparing the base and optimum designs, it can be observed that the platinum loading increases substantially from 0.4 mg/cm^2 to 1.1 mg/cm^2. Similarly the platinum to carbon ratio also increases. This is expected because at low current densities, the fuel cell performance is limited by electrochemical kinetics. However, this increase in catalyst loading occurs at the expense of a reduction in electrolyte and void space which change from 0.5398 and 0.1049 to 0.4294 and 0.09879 respectively. The lower porosity and electrolyte volume fraction result in lower oxygen and proton transport. This should manifest in worse performance at high current densities for the optimal case. In this case, however, this is not observed because the increase in GDL porosity from 0.5 to 0.75 counters this effect by providing a higher oxygen concentration at the GDL—CL interface. Nonetheless, the increase in current density at high current densities is minimal when taking into account that platinum content has more than doubled. This can be observed in the polarization curve in Figure 11.

Figure 12 shows the oxygen molar fraction, solid and electrolyte phase poten-

tials and the volumetric current density at the catalyst layer for the optimum design. Comparing Figures 7 and 12, an increase in oxygen concentration at the GDL/CL interface can be observed due to increased GDL porosity. On the other hand, the negative effect of the increased GDL porosity can be found on the solid phase potential contour plot where a larger voltage drop is observed; therefore, reducing the overpotential. The negative effects are negligible compared to the positive effects of higher oxygen concentrations and the overall result is a homogeneous increase in volumetric current density throughout the catalyst layer.
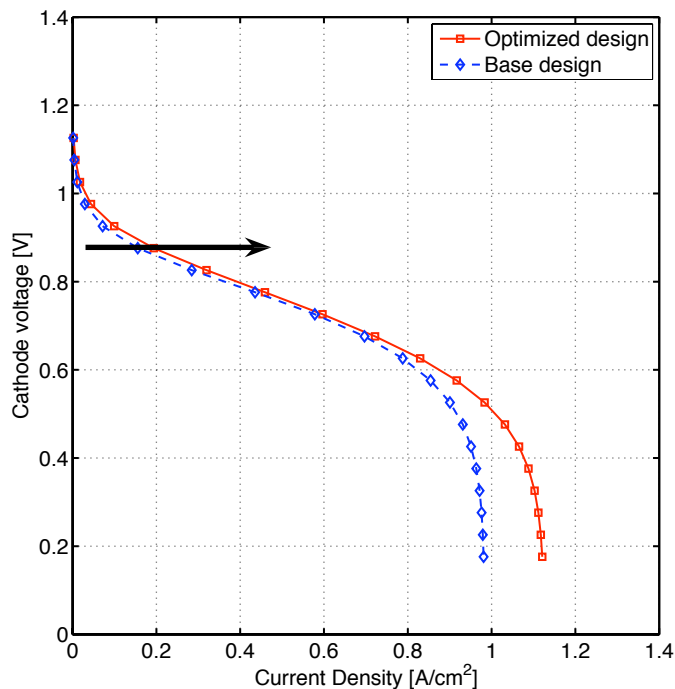

Fig. 11. Polarization curve for the base case and for the optimal design for a voltage across the electrode of 0.3V, i.e. a cell voltage of 0.876 V.

4.3 Optimization at medium current densities

At an electrode voltage of 0.5V, the initial design provides a current density of $0.6966 A/cm^2$. After approximately 2 minutes on a 2 GHz Power Mac G5 and 20 iterations, the optimization algorithm converged to a new design that provides a current density of $0.9445 A/cm^2$. The design variables at this new design are $\{m_{Pt}, \epsilon_{agg}, Pt|C, \epsilon_V^{gdl}\} = \{0.5357, 0.6345, 0.4669, 0.7801\}$. For these values, the volume fractions of solid, electrolyte and void phase are 0.2205, 0.5395 and 0.2400 respectively. Finally, the gradient of the objective function is $\nabla_\lambda \cdot \mathbf{i} = \{6.64e-5, 8.07e-5, -1.58e-4, -6.03e-5\}$ which results in a L_2 norm of 1.99e-04, i.e. almost zero.
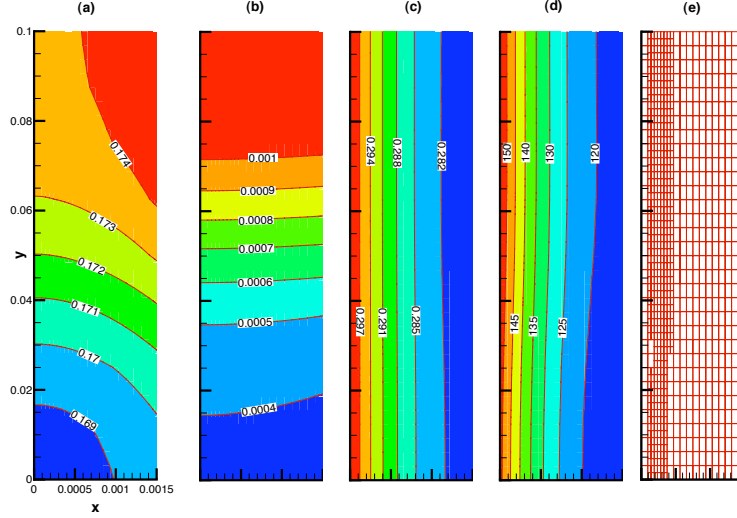
Fig. 12. Contour lines at the catalyst layer for the optimized electrode design at $dV = 0.3V$ for (a) oxygen molar fraction [-], (b) potential in the solid phase [V], (c) potential in the electrolyte [V] and (d) volumetric current density [A/cm^3].

Comparing the design at low and medium electrode voltages, it is easy to observe that the parameters that have changed the most are the platinum loading and the amount of electrolyte as well as the porosity in both CL and GDL. At medium current density, proton and oxygen transport become important whereas the effect of kinetics becomes less significant. For this reason, the platinum loading for the optimized case is reduced to 0.54 mg/cm^2, a much lower value than that obtained from optimization at low current density. The decrease in platinum loading results in a reduction on the solid phase volume fraction which in turn is responsible for the increased CL porosity. The increase in CL porosity increases the effective area available for oxygen dissolution, a_{agg}, and the increase in GDL and CL porosities help to reduce mass transport limitations associated with gas-phase oxygen transport. Finally, the increase in the electrolyte volume fraction results in a reduction in the ohmic losses due to proton transport and mass-transport limitations inside the agglomerate. Figure 13 shows the polarization curve of the optimal and base design. It is clear that performance is enhanced at medium current densities by the reduction on mass-transport limitations and the improved proton conductivity. On the other hand, the performance at low current densities increases very little compared to the base design and has decreased compared to the optimum design at 0.3V. This reduction in performance is due to the reduction in platinum loading from 1.13 to 0.54 mg/cm^2. Finally, the slight differences in performance at low current densities might be due to the increase in porosity in the catalyst layer. Since only the volume fraction of the catalyst layer occupied by agglomerates is used for the reaction, an increase in porosity results in less area available for the reaction. This could explain

26

why an increase in current density with respect to the base case is not observed at low currents even though platinum loading is increased with respect to the base case. This shows the intricate coupling between design variables and highlights the need for numerical optimization.

Figure 14 shows the oxygen mole fraction, solid and electrolyte phase potentials and the volumetric current density at the catalyst layer for the optimum design. Comparing the predictions for the base and optimum design cases in Figures 8 and 14 respectively, it can be observed that the mole fraction of oxygen is increased with respect to the base design. This is due to an increase in the GDL and CL porosity from 0.5 to 0.8 and from 0.1 to 0.2 respectively. This results in a higher oxygen molar fraction at the interface between the GDL and the CL and at the surface of the agglomerates. The increase in GDL porosity implies a corresponding decrease in effective electronic conductivity in the GDL. This effect is manifested as an increase in electronic phase potential at the GDL/CL interface. Simultaneously, in the CL, there is an increase in the ionic phase potential gradient even though the electrolyte volume fraction is the same, mainly due to the increase in current density. The net result is that for the optimized design the local overpotentials are slightly lower than that for base design. However, since the reaction rate (equivalent to current) is dependent on both the oxygen concentration and the overpotential, the slight decrease in overpotential is negligible compared to the effect of increased oxygen concentration. These results demonstrate the complex, intricate coupling among the transport of three different species and the electrochemical reaction. The result is again a quite uniform increase in the volumetric current density even though a slightly higher increased is observed near the membrane, mainly due to the increase in oxygen availability.

4.4 Optimization at high current densities

At an electrode voltage of $0.7V$, the initial design provides a current density of $0.9312A/cm^2$. After 37 iterations, the optimization algorithm converged to a new design that provides a current density of $1.7739A/cm^2$. The design variables at this new design are $\{m_{Pt}, \epsilon_{agg}, Pt|C, \epsilon_V^{gdl}\} = \{0.3029, 0.7600, 0.4670, 0.8341\}$. For these values, the volume fractions of solid, electrolyte and void phase are 0.1246, 0.5296 and 0.3456 respectively. Note that the total electrolyte volume fraction is smaller that the volume fraction in the agglomerate. This is due to the relatively large porosity in the CL. Finally, the gradient of the objective function has an L_2 norm of 8.51e-5, again almost zero.

The optimum design at high current densities results in a platinum loading of $0.3mg/cm^2$. It is well recognized that high current density performance is limited by mass-transport phenomena [10]. Thus the reduced Pt loading results
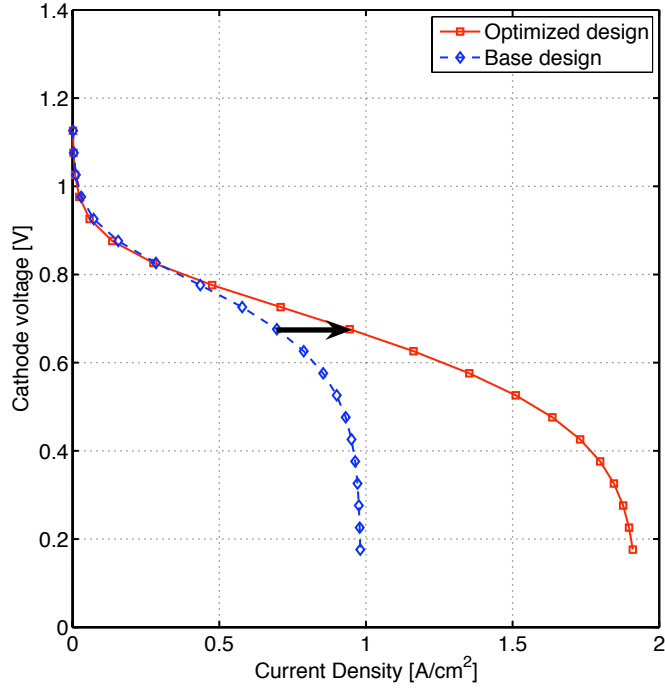
27

Fig. 13. Polarization curve for the base case and for the optimal design for a voltage across the electrode of 0.5V, i.e. a cell voltage of 0.676 V.
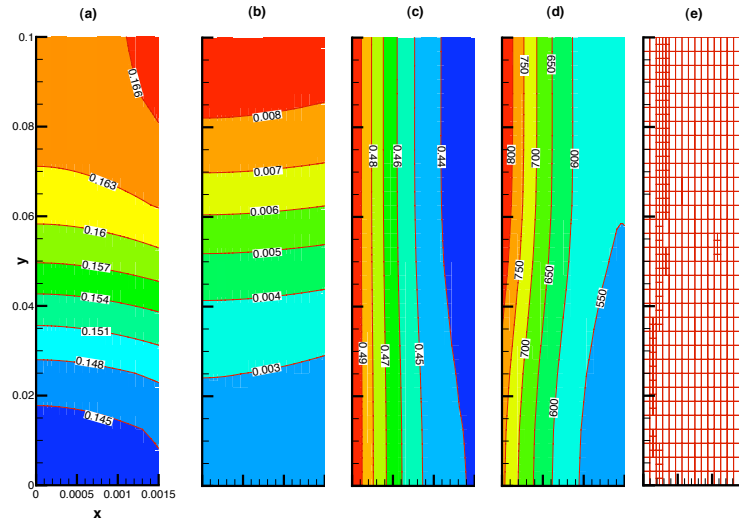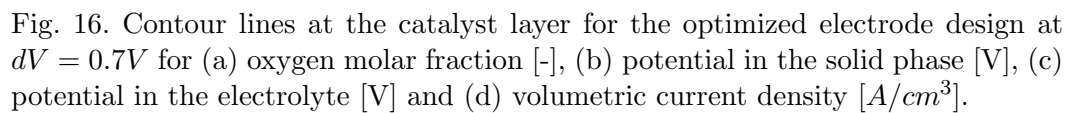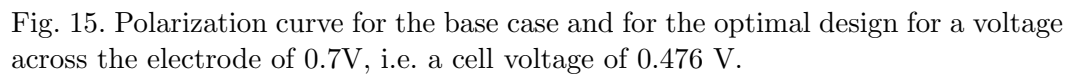

Fig. 14. Contour lines at the catalyst layer for the optimized electrode design at $dV = 0.5V$ for (a) oxygen molar fraction [-], (b) potential in the solid phase [V], (c) potential in the electrolyte [V] and (d) volumetric current density [A/cm^3].

in an increase on the porosity of the catalyst layer. This increase in porosity enhances mass transport by increasing the effective oxygen diffusion coefficient and increasing the area available for oxygen dissolution as illustrated by equation (27). In order to further reduce oxygen transport limitations, the porosity on the GDL is also increased with respect to the optimum design at medium current densities. Comparing the three designs at low, medium and high current densities, it is easy to see the interplay between parameters. Platinum loading and electrolyte content are varied depending on the design operating point to either increase kinetics or reduce mass-transport limitations. Only the platinum to carbon ratio remains almost unchanged. Figure 15 shows the polarization curve of the optimum design and that of the base case. It can be clearly observed that although the optimized design exhibits enhanced performance at high current densities, it has a worse performance than the base case at low current densities. In this case, reducing mass-transport limitations was the main target of the optimization and this was achieved at the cost of a reduction on the active area and; as a consequence, a reduction on the oxygen reaction kinetics.

Figure 16 shows the oxygen molar fraction, solid and electrolyte phase potentials and the volumetric current density at the catalyst layer for the optimum design. Comparing Figures 9 and 16, similar to the findings discussed in the previous section, it can be observed that the molar fraction of oxygen is increased substantially with respect to the base design. This is due to an increase in both the GDL and CL porosity. The voltage drop in the electrolyte is increased even though the electrolyte volume fraction is the same, mainly due to the increase in current density. Similarly, the voltage drop in the solid phase is increased due to an increase in current density as well as a decrease in the solid phase volume fraction in both GDL and catalyst layer. As discussed in section 4.3, even though the overpotential is reduced due to the additional voltage losses, the increase in oxygen molar fraction offset the negative effects and the volumetric current density increases everywhere in the catalyst layer. Furthermore, the increase in volumetric current density is not uniform and the contour plot of the volumetric current density changes substantially with respect to the base case. Comparing the volumetric current generation of the base and optimum design, a larger increase in volumetric currents is obtained near the membrane. This suggests that due to the reduction in mass-transport limitations oxygen gas is now able to reach deep into the catalyst layer. Finally, it is important to mention that even at high current density, CL saturation should not occur. The minimum oxygen molar fraction in Figure 16 is 0.12, this results in a water molar fraction of 0.21, i.e. less than 75% relative humidity.

29

Fig. 15. Polarization curve for the base case and for the optimal design for a voltage across the electrode of 0.7V, i.e. a cell voltage of 0.476 V.

Fig. 16. Contour lines at the catalyst layer for the optimized electrode design at $dV = 0.7V$ for (a) oxygen molar fraction [-], (b) potential in the solid phase [V], (c) potential in the electrolyte [V] and (d) volumetric current density [A/cm^3].

4.5   Effect of the catalyst layer agglomerate structure: agglomerate radius and electrolyte thin film

In the previous studies, the agglomerate structural parameters, i.e. the radius of the agglomerate and the ionomer thin film surrounding the agglomerate, are kept constant throughout the optimization process. In this section, the effect of these parameters on the optimization results are discussed in detail. To discuss these effects, electrode optimization is performed using the data from Table 3 and using three different values for each one of the structural parameters. All the optimization results are obtained for a given voltage across the electrode of 0.5V, i.e. at medium current densities.

Figures 17 and 18 show the optimum design parameters and optimum volume fractions for a catalyst layer with agglomerates of radius 1, 0.5 and 0.25 μm respectively. These three designs provide a current density of 0.9445, 1.2497 and 1.4385 A/cm^2 respectively at a voltage across the electrode of 0.5V. The current density increases monotonically with a reduction on the agglomerate radius. This effect is justified because a reduction in the agglomerate radius mitigates mass transport limitations. This reduction is achieved through two mechanisms. The first mechanism is due to the transport inside the agglomerate. In a large agglomerate, the diffusive path to reach the reaction site is longer and; therefore, the reduction on the radius alleviates the mass transport limitations inside the agglomerate. The second is due to improved oxygen dissolution, since the area available for oxygen dissolution is proportional to the inverse of the agglomerate radius, reducing the radius increases the area available for oxygen dissolution. In terms of the optimal composition, the effect of the agglomerate radius are very well illustrated by Figures 17 and 18. Figure 17 shows that the optimum amount of ionomer inside the agglomerate and the GDL porosity are reduced as the radius of the agglomerate decreases. This is due to the reduced mass transport limitations inside the agglomerate. Figure 18 also illustrates the effect of reduced mass-transport limitations by showing a decrease in the catalyst layer porosity. Comparing Figures 17 and 18 illustrates that, even though the amount of ionomer inside the agglomerate decreases, the total amount of ionomer in the catalyst layer increases slightly. This shows the interaction between the catalyst layer structure and its overall properties. Since the volume of the catalyst layer is the same, having agglomerates with a smaller radius means that more agglomerates are necessary to fill the layer. This results in increased ionomer content. In terms of the optimization problem, the steady increase in current density with agglomerate radius reduction implies that the optimal catalyst layer would have agglomerates that are as small as possible. Therefore, introducing the agglomerate radius as a design variable is unnecessary because the optimization algorithm would just minimize its value. An exception to this rule could occur for very low current densities because mass transport limitations can be ignored.
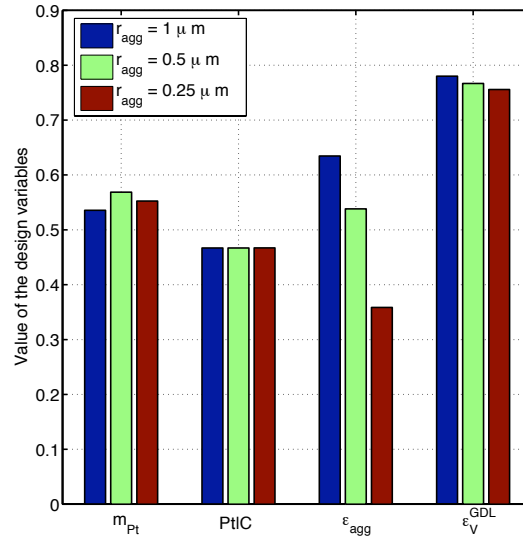
Fig. 17. Bar chart of the optimum parameters for a catalyst layer with an agglomerate radius of 1, 0.5 and $0.25\mu m$.
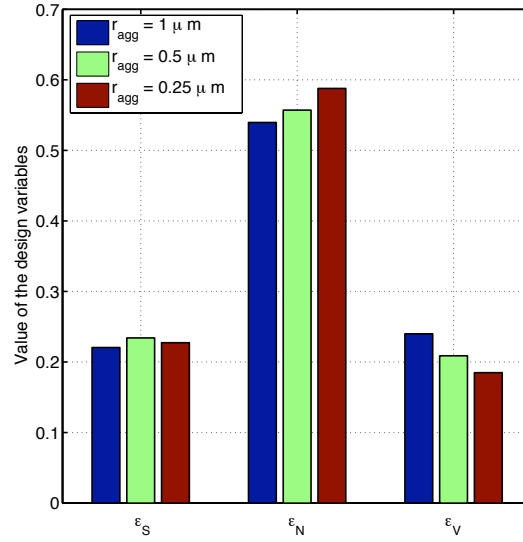

Fig. 18. Bar chart of the optimum catalyst layer composition for a catalyst layer with an agglomerate radius of 1, 0.5 and $0.25\mu m$.

Figures 19 and 20 show the optimum design parameters and optimum volume fractions for a catalyst layer with an ionomer film surrounding the agglomerate of 0.08, 0.04 and $0.0\mu m$ respectively. These three designs provide a current density of 0.9445, 1.1600 and 1.6004 A/cm^2 respectively at a voltage across the electrode of 0.5V. As in the previous case, the current density increases steadily with a reduction in the ionomer film surrounding the agglomerate which in turn allows the optimum design to increase its platinum loading

and therefore provide the increase in current density. Again, this effect is explained by a reduction on the mass transport limitations. In this case, a thinner film means that the oxygen needs to diffuse through a shorter path before reaching the reaction sites. This effect is illustrated by the evolution of the optimum compositions. Figure 20 shows a notable decrease in the catalyst layer porosity. This reduction frees up space inside this layer that is used to increase the platinum content. Figure 19 illustrates a major difference between this parametric study and the previous one. In this case, the ionomer content inside the agglomerate is increased instead of decreased. This highlights the different nature of the transport resistances. Reducing the thin film increases the amount of oxygen available at the surface of the agglomerate. Then, to take advantage of the increased oxygen mole fraction, the ionomer content is increased to enhance the transport of the additional oxygen to the interior of the agglomerate. As in the previous case, this study suggest that adding the ionomer film to the optimization process has no additional benefit since this value would just be reduced to zero during the optimization process.

In summary, the study shows that both radius of the agglomerate and ionomer film thickness are mass transport limiting processes that are introduced by the current structure of catalyst layers. Elimination of these limitations will most certainly enhance catalyst layer performance, however, these limitations are difficult to either control or eliminate with current manufacturing methods. Structured catalyst layers are likely to provide a solution to these problems by allowing control of the ionomer film and agglomerate radius.
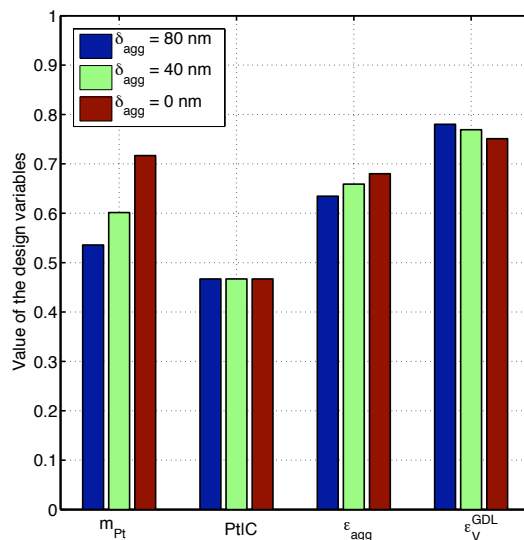

Fig. 19. Bar chart of the optimum parameters for a CL with an ionomer film surrounding the agglomerate of 0.08, 0.04 and $0.0 \mu m$.
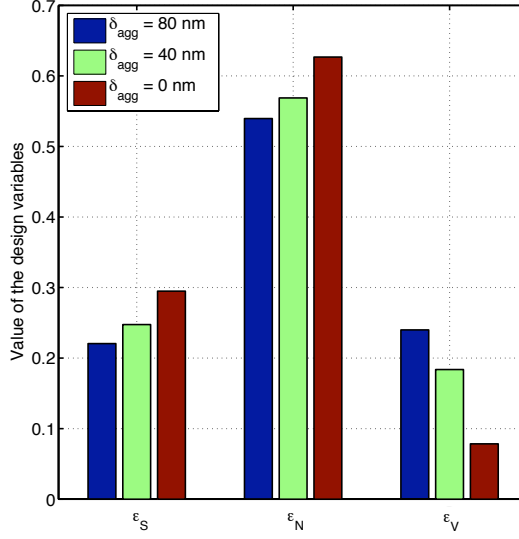
33

Fig. 20. Bar chart of the optimum catalyst layer composition for a CL with an ionomer film surrounding the agglomerate of 0.08, 0.04 and $0.0\mu m$.

4.6 Further discussion

A bar chart summarizing the optimum design parameters for the three cases studied: agglomerate model at 0.3V, 0.5V and 0.7V across the electrode is shown in Figure 21. This figure illustrates the trends the optimum design exhibits when the operating conditions shift to higher current densities: a reduction in platinum loading and an increase in electrolyte content and GDL porosity. Also, a constant value for the platinum to carbon weight ratio is observed for all current densities and independently of the model used.

A bar chart illustrating the optimal volume fraction composition of the catalyst layer for the three cases studied is shown in Figure 22. This figure also highlights the main trends in the optimal composition as the operating current for optimization is increased: a noticeable increase in porosity, a decrease on the solid phase volume fraction and a maximum ionomer content at medium current densities - in the ohmic region of the polarization curve.

To conclude the discussion, the results obtained from this paper are compared with experimental data. In the past decade, several studies [40–44,30,28] have suggested that an ionomer content in the the range of 30 to 40%wt. in the catalyst layer provides the best polarization curves for oxygen as well as air fed fuel cells over a large range of operating conditions. Transforming the previous ionomer volume fraction to weight fraction using the equations in reference [46], the optimal ionomer weight fractions in the catalyst layer for the agglomerate are 34.1%wt., 58.5% wt. and 71.0 % wt. respectively. At a
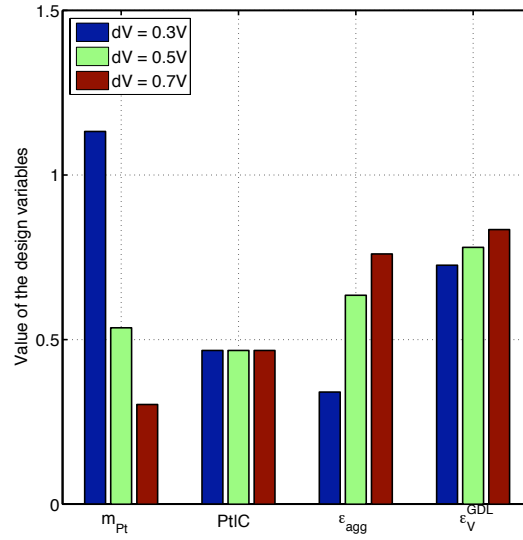
Fig. 21. Bar chart of the optimum parameters for the catalyst layer composition obtained using the agglomerate model at 0.3, 0.5 and 0.7V.
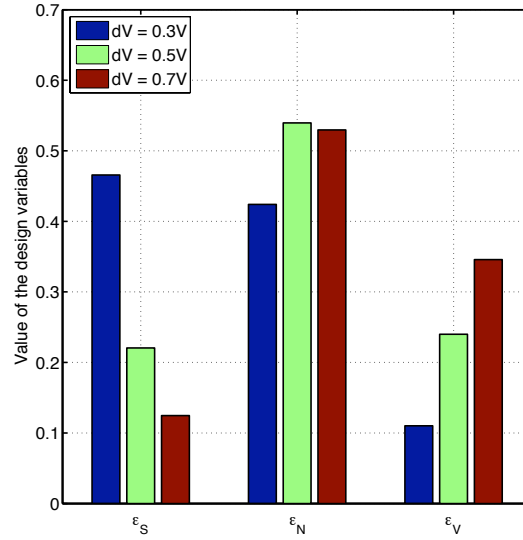

Fig. 22. Bar chart of the optimum catalyst layer composition obtained using the agglomerate model at 0.3, 0.5 and 0.7V.

first glance, the results suggest an unrealistic ionomer mass fraction at high current density.

A closer examination at the method used to obtain the optimal ionomer content shows that this issue is not straightforward. In the studies presented in the literature [40–44,30,28], the platinum content and the platinum to carbon ratio are kept constant. Therefore, if the catalyst layer thickness is fixed, the

solid volume fraction also remains constant as shown by equation (7). In most of the studies, the catalyst layer thickness is not reported and as a result, the solid phase volume fraction cannot be obtained. However, Gode et al. [28] reported minimal changes in catalyst layer thickness with changes in ionomer content. Fortunately, Gode et al. [28] and Xie et al. [44] both report the solid phase volume fraction for catalyst layer with different ionomer contents. The solid volume fraction is indeed almost constant with values in the range of 30 to 50%. As a result of the constant solid phase, increasing the ionomer content results in a reduction in porosity.

Revisiting Figure 22, we note the methodology in the optimization algorithm to increase performance differs from that in the experimental studies. In the numerical optimization procedure, the solid phase is not constrained to remain constant and is in fact reduced substantially from about 40% at low currents to values of around 10 to 20% at high currents. This reduction in solid phase creates additional space in the catalyst layer which is then used to increase both the ionomer content and the overall catalyst layer porosity. The apparent discrepancies between experimental results and the optimization results are due to the differences in solid phase volume fractions. In figure 22, the solid phase volume fraction is in the range of 30 to 50% in case 1. This case corresponds to optimal ionomer contents of 34.1%wt, i.e. within the range of the values reported in the literature. Cases 2 and 3 have solid volume fractions of 22% and 12 % and this results in higher ionomer mass fractions of 58.5% wt. and 71.0 % wt. respectively. These results are also consistent with data presented by Sasinkumar et al.[47] who reported that the optimum Nafion content increases with decreasing platinum loading, which, assuming the catalyst layer thickness to be constant, results in a reduction of the solid phase volume fraction. Furthermore, examining the polarization curves reported by Sasinkumar et al., we observe better performance at high current densities with platinum loadings of $0.1mg/cm^2$ (optimal ionomer content of 50% wt) and 0.25 mg/cm^2 (optimal ionomer content of 40% wt) than at platinum loadings of $0.5mg/cm^2$ where mass-transport limitations are evident. This again confirms our findings.

The results from this study and the above discussion suggest the optimal ionomer content is dependent on the solid phase volume fraction. It would thus be most useful in future experimental studies to document simultaneously the thickness of the catalyst layer and the volume fractions of solid, as well as ionomer and void space. The present findings also suggest that the experimentally identified optimal ionomer content of 30-40%wt. is only optimal for a given solid phase volume fraction of 30 to 50%. Future experimental studies should be performed to investigate the effect of reducing the solid phase volume fraction and increasing the ionomer content to confirm if indeed further increase in ionomer content would result in further improvements in performance at high current densities, as suggested by the agglomerate model

predictions. Remarkably, if such performance gains are realized, they would have no associated cost penalty. Instead, they most likely would reduce the amount of platinum required in the catalyst layer.

5   Conclusions

A method to obtain optimum design parameters, such as catalyst loading, GDL and CL porosity, and $Pt|C$ ratio for PEMFC cathodes, was presented. The catalyst layer is described via an agglomerate model expanded to account for parameters that relate the catalyst ink composition to the catalyst layer microstructural features. The governing equations of this model and its sensitivity equations are solved using an adaptive finite element method.

Using the model and its sensitivities, three optimization problems are solved to obtain the optimal cathode composition at different current densities - representing the activation, ohmic, and mass-transport dominated regions of the fuel cell polarization behavior. The results show that the optimum cathode composition depends on current density. An optimal cathode is thus application dependent and should be obtained by taking into consideration the design operating conditions. If a specific application requires operation at different points of the polarization curve, a multi-objective optimization problem would need to be solved with appropriate weights for each current density.

The effect of microstructural catalyst layer parameters in the optimum design is also studied. The study shows that both radius of the agglomerate and ionomer film thickness are mass transport limiting processes that are introduced by the current structure of catalyst layers. Thus, elimination of these limitations will most certainly enhance catalyst layer performance and they do not need to be included in the optimization process since they will always be reduced to its minimum value.

The optimization results are evaluated with respect to experimental data. The evaluation brings to light some of the limitations in experimental studies performed to date which were constrained to a narrow range of volume fractions of electronically conducting material. The analysis suggests that further improvements in catalyst layer performance at medium and high current density might be possible by reducing carbon and platinum loading to achieve solid phase volume fraction of 10-20% and increasing the electrolyte content to achieve volume fractions of 45-55% in the catalyst layer. These results need to be corroborated by further experimental studies.

Finally, the current model addresses only the cathode design and does not account for species transport within the membrane or the effect of anode pro-

cesses and operating conditions. The anode operating conditions and water transport might influence the design by either decreasing or increasing the water content in the cathode catalyst layer due to back-diffusion or electro-osmotic drag respectively. Future work by the authors will focus on the development of a membrane and anode model to allow coupled optimization of both anode and cathode simultaneously.

6 Acknowledgments

Nomenclature

α_c — transfer coefficient, [-]

δ_{agg} — thin electrolyte film surrounding the agglomerate, $[\mu m]$

ϵ_N^{cl} — electrolyte phase volume fraction in the catalyst layer, [-]

ϵ_S^{cl} — solid phase volume fraction in the catalyst layer, [-]

ϵ_V^{cl} — porosity or void volume fraction in the catalyst layer, [-]

ϵ_S^{gdl} — solid phase volume fraction in the GDL, [-]

ϵ_V^{gdl} — porosity or void volume fraction in the GDL, [-]

ϵ_{agg} — volume fraction of ionomer inside the agglomerate, [-]

γ — coefficient in Tafel equation, [-]

$\hat{n}$ — number of agglomerates inside the catalyst layer, [-]

$\hat{N}_{O_2}$ — oxygen flux through the agglomerate boundary, $[mol \cdot cm^{-2} \cdot s^{-1}]$

ϕ_0 — membrane potential at the membrane - catalyst layer interface, [V]

ϕ_L — Thiele's modulus, [-]

ϕ_m — membrane potential, [V]

ϕ_S — solid phase potential, [V]

ρ_c — Carbon density, $[g \cdot cm^{-3}]$

ρ_{Pt} — Platinum density, $[g \cdot cm^{-3}]$

σ_m^{eff-cl} — effective electrolyte conductivity in the catalyst layer, $[S \cdot cm^{-1}]$

σ_S^{eff-cl} — effective solid phase conductivity in the catalyst layer, $[S \cdot cm^{-1}]$

$\sigma_m^{eff-gdl}$ — effective electrolyte conductivity in the GDL, $[S \cdot cm^{-1}]$

$\sigma_S^{eff-gdl}$ — effective solid phase conductivity in the GDL, $[S \cdot cm^{-1}]$

A_0 — catalyst surface area per unit mass of the catalyst particle, $[cm^2 g^{-1}]$

A_v — area utilized for the oxygen reduction reaction per unit volume of catalyst layer, $[cm^2/cm^3]$

a_{agg} ratio between the effective surface area usable to dissolve oxygen into the agglomerate and the catalyst layer volume, $[cm^2/cm^3]$

$c_{O_2}^{ref}$ reference oxygen concentration, $[mol \cdot cm^{-3}]$

$c_{O_2,g-l}$ concentration of dissolved oxygen at the surface of the electrolyte, $[mol \cdot cm^{-3}]$

$c_{O_2,l-s}$ concentration of dissolved oxygen at the electrolyte solid interface, $[mol \cdot cm^{-3}]$

c_{tot} concentration of the mixture of air and water vapour, $[mol \cdot cm^{-3}]$

D^{eff} effective oxygen diffusion coefficient inside the agglomerate, $[cm^2 \cdot s^{-1}]$

$D_{O_2,N}$ diffusion coefficient of oxygen in Nafion, $[cm^2 \cdot s^{-1}]$

D_{O_2} oxygen diffusion coefficient in nitrogen, $[cm^2 \cdot s^{-1}]$

$D_{O_2}^{eff-cl}$ effective oxygen diffusion coefficient in the catalyst layer, $[cm^2 \cdot s^{-1}]$

$D_{O_2}^{eff-gdl}$ effective oxygen diffusion coefficient in the GDL, $[cm^2 \cdot s^{-1}]$

dV applied voltage to the electrolyte, $[V]$

E_r effectiveness factor, [-]

F Faraday constant, 96493 $[C \cdot mol]$

$H_{O_2,N}$ Henry's law constant for the dissolution of oxygen into the electrolyte, $[\frac{Pa \cdot cm^3}{mol}]$

i current density, $[A \cdot cm^{-2}]$

i_0^{ref} exchange current density, $[A \cdot cm^{-2}]$

k_c reaction rate constant, $[s^{-1}]$

L catalyst layer thickness, $[cm]$

L^{gdl} gas diffusion layer thickness, $[cm]$

m_{Pt} catalyst platinum mass loading per unit area on the catalyst, $[g \cdot cm^{-2}]$

n number of agglomerates per unit volume, $[\mu m^{-3}]$

p_{O_2} partial pressure of oxygen, $[Pa]$

p_{tot} pressure of the mixture, $[Pa]$

PtC mass percentage of platinum catalyst on the support carbon black, [-]

R gas constant, 8.315 $[J \cdot K^{-1} \cdot mol^{-1}]$

r_{agg} radius of the agglomerate, $[\mu m]$

R_{O_2} oxygen reaction rate, $[mol \cdot cm^{-2}s^{-1})]$

S_{agg} surface of the agglomerate, $[cm^2]$

T temperature, $[K]$

$x_{O_2}^0$ oxygen molar fraction in the channel, [-]

x_{O_2} oxygen molar fraction, [-]

References

[1] D.M. Bernardi and M.W. Verbrugge. Mathematical model of a gas diffusion electrode bonded to a polymer electrolyte. *AIChE Journal*, 37(8):1151–1163, August 1991.

[2] D. M. Bernardi and M. W. Verbrugge. Mathematical model of the

solid-polymer-electrolyte fuel cell. *Journal of the Electrochemical Society*, 139(9):2477–2491, September 1992.

[3] C. Marr and X. Li. Composition and performance modelling of catalyst layer in a proton exchange membrane fuel cell. *Journal of Power Sources*, 77(1):17–27, January 1999.

[4] D. Song, Q. Wang, Z. Liu, T. Navessin, M. Eikerling, and S. Holdcroft. Numerical optimization study of the catalyst layer of pem fuel cell cathode. *Journal of Power Sources*, 126(1-2):104–111, 2004.

[5] M. Eikerling and A.A. Kornyshev. Modelling the performance of the cathode catalyst layer of polymer electrolyte fuel cells. *Journal of Electroanalytical Chemistry*, 453(1-2):89–106, August 1998.

[6] D. Bevers, M. Wohr, K. Yasuda, and K. Oguro. Simulation of a polymer electrolyte fuel cell electrode. *Journal of Applied Electrochemistry*, 27(11):1254–1264, November 1997.

[7] A.A. Kulikovsky, J. Divisek, and A.A. Kornyshev. Modeling the cathode compartment of polymer electrolyte fuel cells: Dead and active reaction zones. *Journal of the Electrochemical Society*, 146(11):3981–3991, November 1999.

[8] L. You and H. Liu. A parametric study of the cathode catalyst layer of PEM fuel cells using a pseudo-homogeneous model. *International Journal of Hydrogen Energy*, 26(9):991–999, September 2001.

[9] Y.W. Rho, S. Srinivasan, and Y.T. Kho. Mass transport phenomena in proton exchange membrane fuel cells using O2/He, O2/Ar, and O2/N2 mixtures. II. theoretical analysis. *Journal of the Electrochemical Society*, 141(8):2089–2096, August 1994.

[10] W. Sun, B. A. Peppley, and K. Karan. An improved two-dimensional agglomerate cathode model to study the influence of catalyst layer structural parameters. *Electrochimica Acta*, 50(16-17):3347–3358, 2005.

[11] S.J. Ridge, R.E. White, Y. Tsou, R.N. Beaver, and G.A. Eisman. Oxygen reduction in a proton exchange membrane test cell. *Journal of the Electrochemical Society*, 136(7):1902–1909, July 1989.

[12] N.P. Siegel, M.W. Ellis, D.J. Nelson, and M.R. Von Spakovsky. Single domain PEMFC model based on agglomerate catalyst geometry. *Journal of Power Sources*, 115(1):81–89, March 2003.

[13] K. Broka and P. Ekdunge. Modelling the PEM fuel cell cathode. *Journal of Applied Electrochemistry*, 27(3):281–289, March 1997.

[14] P.-C. Sui, L.-D. Chen, James P. Seaba, and Yoshinori Wariishi. Modeling and optimization of a PEMFC catalyst layer. In *SAE SP-1425, Fuel Cell for Transportation*. SAE, 1999. 1999-01-0539.

[15] A. Z. Weber and J. Newman. Modeling transport in polymer-electrolyte fuel cells. *Chemical Reviews*, 104(10):4679–4726, October 2004.

[16] T. Berning, D.M. Lu, and N. Djilali. Three-dimensional computational analysis of transport phenomena in a pem fuel cell. *Journal of Power Sources*, 106(1-2):284–294, 2002.

[17] T. Berning and N. Djilali. Three-dimensional computational analysis of transport phenomena in a pem fuel cell - a parametric study. *Journal of Power Sources*, 124(2):440–452, 2003.

[18] M. Grujicic, C.L. Zhao, K.M. Chittajallu, and J.M. Ochterbeck. Cathode and interdigitated air distributor geometry optimization in polymer electrolyte membrane (PEM) fuel cells. *Materials Science and Engineering B*, 108:241–252, 2004.

[19] M. Grujicic and K.M. Chittajallu. Design and optimization of polymer electrolyte membrane (PEM) fuel cells. *Applied surface science*, 227:56–72, 2004.

[20] M. Grujicic and K.M. Chittajallu. Optimization of the cathode geometry in the polymer electrolyte membrane (PEM) fuel cells. *Chemical Engineering Science*, 59:5883–5895, 2004.

[21] Frédéric Jaouen, Göran Lindbergh, and Göran Sundholm. Investigation of mass-transport limitations in the solid polymer fuel cell cathode - I. Mathematical model. *Journal of the Electrochemical Society*, 149(4):A437–A447, 2002.

[22] R. B. Bird, W. E. Stewart, and E.N. Lightfoot. *Transport Phenomena*. J. Wiley and Sons, 2nd edition, 2002.

[23] J.G.Pharoah, D. Harvey, and K. Karan. Comparision of catalyst treatements for PEM fuel cell modelling. In *4th ASME Conference on Fuel Cell Science, Engineering and Technology*, Irvine, California, June 19-21 2006.

[24] M. Secanell, B. Carnes, A. Suelman, and N. Djilali. Numerical optimization of proton exchange membrane fuel cell cathodes. *Electrochimica Acta*, 52(7):2668–2682, February 2007.

[25] S. Litster and G. McLean. PEM fuel cell electrodes. *Journal of Power Sources*, 130(1-2):61–76, May 2004.

[26] Tuanhong Zhou and Hongtan Liu. Effects of the electrical resistances of the gdl in a pem fuel cell. *Journal of Power Sources*, 161(1):445–453, October 2006.

[27] J.G. Pharoah, K. Karan, and W. Sun. On effective transport coefficients in pem fuel cell electrodes: Anisotropy of the porous transport layers. *Journal of Power Sources*, 161(1):214–224, October 2006.

[28] Peter Gode, Frédéric Jaouen, Göran Lindbergh, Anders Lundblad, and Göran Sundholm. Influence of the compositon on the structure and electrochemical characteristics of the pemfc cathode. *Electochimica Acta*, 48:4175–4187, 2003.

[29] K. Karan. Assessment of transrpot-limited catalyst utilization for engineering of ultra-low pt loading polymer electrolyte fuel cell anodes. *Electrochemistry Communications*, In Press, doi:10.1016/j.elecom.2006.10.057, 2006.

[30] S.J. Lee, S. Mukerjee, J. McBreen, Y.W. Rho, Y.T. Kho, and T.H.Lee. Effects of nafion impregnation on performances of pemfc electrodes. *Electrochimica Acta*, 43(24):3693–3701, 1998.

[31] D. Song, Q. Wang, Z. Liu, T. Navessin, and S. Holdcroft. Numerical study of pem fuel cell cathode with non-uniform catalyst layer. *Electochimica Acta*, 50:731–737, 2004.

[32] David G. Luenberger. *Optimization by vector space methods*. John Wiley & Sons, New York, 1969.

[33] K. Yosida. *Functional analysis*. Springer-Verlag, Berlin, 1965.

[34] W. Bangerth, R. Hartmann, and G. Kanschat. `deal.II` *Differential Equations Analysis Library, Technical Reference.*

[35] T. A. Davis. A column pre-ordering strategy for the unsymmetric-pattern multifrontal method. *ACM Transactions on Mathematical Software*, 30(2):165–195, 2004.

[36] T. A. Davis. Algorithm 832: Umfpack, an unsymmetric-pattern multifrontal method. *ACM Transactions on Mathematical Software*, 30(2):196–199, June 2004.

[37] B. Carnes and N. Djilali. Systematic parameter estimation for PEM fuel cell models. *Journal of Power Sources*, 144(1):83–93, June 2005.

[38] D.G. Cacuci. *Sensitivity and Uncertainty Analysis: Theory*, volume 1. Chapman and Hall/CRC, Boca Raton, Florida, USA, 2003.

[39] M.S. Eldred, A.A. A.A. Giunta, B.G. van Bloemen Waanders, Jr. S.F. Wojtkiewicz, W.E. Hart, and M.P. Alleva. Dakota, a multilevel parallel object-oriented framework for design optimization, parameter estimation, uncertainty quantification, and sensitivity analysis. version 3.0 users manual. Technical Report 2001-3796, Sandia National Laboratory, 2003.

[40] E. Antolini, L. Giorgi, A. Pozio, and E. Passalacqua. Influence of nafion loading in the catalyst layer of gas-diffusion electrodes for pemfc. *Journal of Power Sources*, 77:136–142, 1999.

[41] E. Passalacqua, F. Lufrano, G. Squadrito, A. Patti, and L. Giorgi. Nafion content in the catalyst layer of polymer electrolyte fuel cells: effects on structure and performance. *Electochimica Acta*, 46:799–805, 2001.

[42] Jian Xie, Karren L. More, Thomas A. Zawodzinski, and Wayne H. Smith. Porosimetry of meas made by "thin film decal" method and its effects on performance of PEFCs. *Journal of the Electrochemical Society*, 151(11):A1841–A1846, 2004.

[43] Guangchun Li and Peter G. Pickup. Ionic conductivity of PEMFC electrodes. *Journal of the Electrochemical Society*, 150(11):C745–C752, 2003.

[44] Zhong Xie, Titichai Navessin, Ken Shi, Robert Chow, Qianpu Wang, Datong Song, Bernhard Andreaus, Michael Eikerling, Zhongsheng Liu, and Steven Holdcroft. Functionally graded cathode catalyst layers for polymer electrolyte fuel cells. II. experimental study of the effects of nafion distribution. *Journal of the Electrochemical Society*, 152(6):A1171–A1179, 2005.

[45] E. L. Cussler. *Diffusion : Mass Transfer in Fluid Systems*. Cambridge University Press, 2nd edition, 1997.

[46] Qianpu Wang, Michael Eikerling, Datong Song, Zhongsheng Liu, Titichai Navessin, Zhong Xie, and Steven Holdcroft. Functionally graded cathode catalyst layers for polymer electrolyte fuel cells. I. theoretical modeling. *Journal of the Electrochemical Society*, 151(7):A950–A957, 2004.

[47] G. Sasikumar, J.W. Ihm, and H. Ryu. Optimum Nafion content in PEM fuel cell electrodes. *Electrochimica Acta*, 50(2-3):601–605, 2004.